Check for updates

Evidence of Hydrocarbon Generation and Overpressure Development in an Unconventional Reservoir Using Fluid Inclusion and Stable Isotope Analysis From the Early Triassic, Western Canadian Sedimentary Basin

Andrew Kingston[1]*, Omid H. Ardakani[1], Elizabeth Watt[2] and Iain M. Samson[3]

[1]Geological Survey of Canada, Natural Resources Canada, Calgary, AB, Canada, [2]ConocoPhilips Canada, Calgary, AB, Canada, [3]School of the Environment, University of Windsor, Windsor, ON, Canada

Deep burial of sedimentary basins results in the development of complex diagenetic environments influenced by pressure, temperature, and metasomatic chemical processes. Fracture systems resulting from deep tectonic-related burial can provide archives of physio-chemical characteristics during burial helping unravel diagenetic events such as hydrocarbon migration and paleobarometry. The Early Triassic Montney Formation in the Western Canadian Sedimentary Basin is a highly productive unconventional hydrocarbon reservoir that has undergone multiple phases of tectonic-related burial and uplift resulting in the formation of a series of calcite-filled fracture systems. These fracture systems occur as vertical to sub-vertical fractures, brecciated zones, and horizontal bedding-plane parallel fractures that are rich in co-occurring, but not co-genetic aqueous and petroleum fluid inclusion assemblages. Fluid inclusion microthermometry, Raman spectroscopy, and stable isotope analysis of these fracture systems and host rock reveals paleobarometric and temperature conditions during fracture formation. Vertical fractures formed at temperatures exceeding 142°C during peak burial associated with the Laramide orogeny ~50 Ma. Similarities in modeled oxygen isotope values of calcite parent fluids and pore water implicate locally sourced carbonate in fracture calcite. Therefore, low permeability and closed system-like conditions were prevalent throughout initial fracture formation and cementation. Petrographic analysis of brecciated and horizontal fractures show evidence of hydrocarbon generation and migration into fracture-filling calcite. Modeling of petroleum inclusion paleobarometry indicates entrapment pressures approaching or even exceeding lithostatic pressure consistent with the development of overpressure associated with the thermal maturation of organic matter following peak burial. Combined use of aqueous and petroleum fluid inclusions in this deeply buried sedimentary system offers a powerful tool for better understanding diagenetic fluid flow, the timing of hydrocarbon migration/maturation, and helps constrain the pressure-temperature history important for characterizing economically important geologic formations.

1 INTRODUCTION

Unravelling the diagenetic history within deeply buried sedimentary systems is an essential component to understanding how processes such as tectonic activity, fluid migration, and hydrocarbon maturation evolved in the basin. These processes can result in the formation of fractures providing records of the physio-chemical conditions during their formation. Fractures in sedimentary rocks form as a result of stress and strain, related to the response of a rock undergoing lithostatic, tectonic, thermal stress, or high-pressure fluids (e.g., Hubbert and Willis, 1957; Cosgrove, 1995; National Research Council, 1996; Lai et al., 2021). Due to the intrinsic relationship between fractures and economically important petroleum and mineral systems, assessing their composition and characterizing parent fluids within these systems is essential for understanding their role in subsurface fluid flow.

Fluid inclusions can play a vital role as they provide pressure-temperature and geochemical snapshots of these vein forming fluids, including primary vein forming fluids, but also subsequent fluids that migrate through these fractures (Roedder, 1984). Parent fluids captured within inclusions provide direct evidence of fluid composition, while microthermometric analysis can provide evidence of pressure-temperature conditions during entrapment (e.g. Roedder, 1984; Goldstein, 2001; Dubessy et al., 2001; Goldstein et al., 2003; Burruss, 2003; Bakker, 2018). This evidence, coupled with burial history models, can also help elucidate the timing of entrapment (Gao et al., 2017; Gasparrini et al., 2021). Therefore, detailed analysis of fluid inclusion assemblages can unravel complex diagenetic histories within structurally complex systems. In addition, petroleum fluid inclusions provide valuable archives of the properties, distribution, and evolution of hydrocarbons in the subsurface and when used in conjunction with aqueous fluid inclusions can provide pressure-temperature history of their host reservoir (Pironon and Bourdet, 2008; Volk and George, 2019).

The lower Triassic Montney Formation is one of the most productive unconventional reservoirs in Canada (National Energy Board, 2013). As a consequence, it has been cored and studied extensively, providing a large collection of material for analysis. However, owing to its complex diagenetic history (Liseroudi et al., 2020, 2021; Vaisblat et al., 2021), regional inconsistencies, and variable tectonic history (Wozniakowska et al., 2021), more work is needed to better characterize this economically important resource. Unconventional systems associated with low-permeability conditions exhibit closed system-like behaviour (Cesar et al., 2020) and often can be overpressured. Fluid inclusions provide a history of formation pressure and temperature and are therefore instrumental in understanding past diagenetic phases in unconventional petroleum reservoirs (Pironon and Bourdet, 2008; Gao et al., 2017). To date only one study has evaluated fluid inclusions in fractures within the Montney Formation (Gasparrini et al., 2021), however extensive work

has been conducted on fluid inclusions within the Devonian and Mississippian strata of the Western Canadian Sedimentary Basin (e.g. Al-Aasm and Clarke, 2004; Al-Aasm et al., 2019 and references within; Davies and Smith, 2006; Yang et al., 2001). Devonian strata exhibit widespread evidence of hydrothermal alteration via the occurrence of saddle dolomite and high temperature alteration of organic matter (Davies and Smith, 2006), distinguishing characteristics that are not observed in the Montney Formation in British Columbia. Therefore, more work is needed to better constrain this diagenetically active system. Lastly, deciphering diagenetic history aids in distinguishing diagenetic from primary geochemical signatures, which is essential in the evaluation of paleoenvironmental versus post-depositional alteration geochemistry including primary versus migrated hydrocarbons (e.g., Ardakani et al., 2020b).
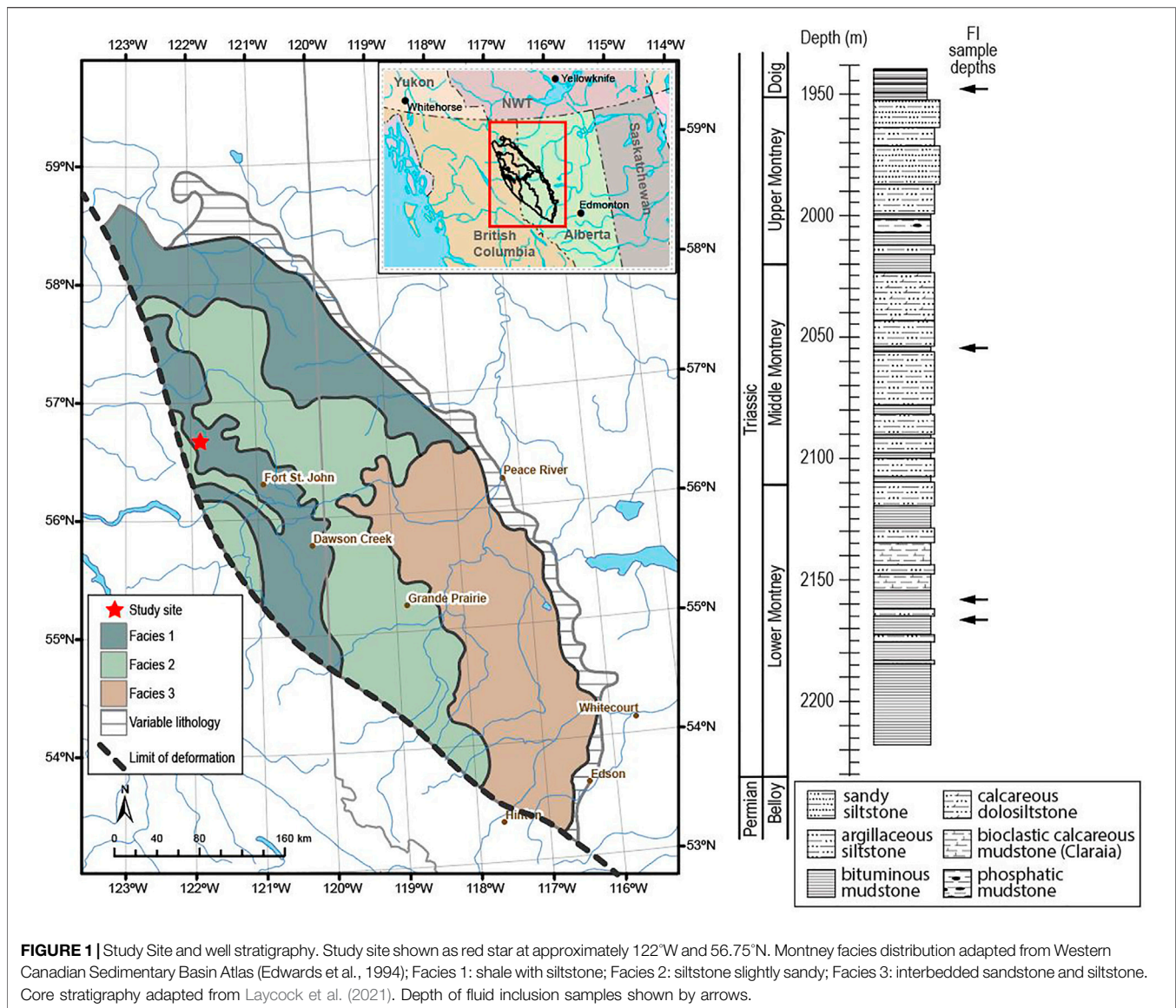
In this study, we use a combination of fluid inclusion microthermometry, stable isotope geochemistry, and Raman spectroscopy to evaluate the fluid sources and pressure-temperature conditions in which calcite-filled fractures formed in the Montney Formation. Modeling of the aqueous and petroleum inclusions reveals the physio-chemical characteristics of the system including the sources of parent fluids and development of overpressure. Finally we assess the implications for the evolution of hydrocarbon maturation and migration in the Montney Formation.

2 GEOLOGICAL SETTING

Sample material for this study was collected from a core of the Montney Formation within the Western Canadian Sedimentary Basin (WCSB) (**Figure 1**). Development of the abundant mineralized fractures within this core may be associated with one of several post-depositional events between the mid-Triassic and Eocene such that a brief overview of the history of the WCSB is provided for context.

The WCSB is a westward-thickening sedimentary wedge that is up to 6 km thick adjacent to the fold-and-thrust belt of the present-day Canadian Rocky Mountains in the west; and which thins to an erosional edge in the east on the Canadian Shield (Price, 1994; Wright et al., 1994; Tufano and Pietras, 2017). The fold-and-thrust belt of the Rocky Mountains of the Canadian Cordillera was shaped over four tectonic pulses from Late Jurassic to Late Cretaceous, each corresponding to a depositional pattern in the nearby foreland basin (Pană and van der Pluijm, 2014). Paleogeographically, the Montney Formation of the WCSB was deposited on a clastic ramp along the northwestern margin of the Pangea Supercontinent (Golonka, 2007) in the Peace River Embayment (PRE) (Barclay et al., 1990) in a collisional retro-foreland basin (Rohais et al., 2018).

The Montney Formation unconformably overlies the Late Permian Belloy Formation and is unconformably overlain by

FIGURE 1 | Study Site and well stratigraphy. Study site shown as red star at approximately 122°W and 56.75°N. Montney facies distribution adapted from Western Canadian Sedimentary Basin Atlas (Edwards et al., 1994); Facies 1: shale with siltstone; Facies 2: siltstone slightly sandy; Facies 3: interbedded sandstone and siltstone. Core stratigraphy adapted from Laycock et al. (2021). Depth of fluid inclusion samples shown by arrows.

organic-rich shales of the Middle Triassic Doig Formation, or the Lower Jurassic Gordondale Member of the Fernie Formation in British Columbia and Alberta, respectively (Davies et al., 2018; Zonneveld and Moslow, 2018). In the distal western part of the basin, the Montney Formation entails offshore transition and offshore organic-rich siltstones as well as turbidite deposits where the Montney Formation is overlain by the Lower Doig organic-rich phosphatic zone Davies et al., 2018).

The Montney Formation is divided into three informal submembers: the Lower Montney, Middle Montney, and Upper Montney Members separated by the Dienerian-Smithian and Smithian-Spathian stage boundaries (Davies, 1997; Davies et al., 2018; Zonneveld and Moslow, 2018). The Lower Montney Formation occurs throughout the WCSB and primarily consists of fine-to medium-grained, laminated bituminous dolomitic siltstone. The Middle

Montney Formation represents a thick succession of bituminous dolomitic siltstone and minor fine-grained sandstone with a low abundance of bioturbation. The Upper Montney consists of a thick succession of fine-to coarse-grained, bituminous, dolomitic siltstone, and it is completely removed due to erosion throughout much of the Alberta portion of the basin (Zonneveld and Moslow, 2018).

Deposition of the Montney Formation was significantly influenced by paleostructural elements in the Peace River area including: the underlying Upper Devonian Leduc reefs, the Hines Creek-Fort St. John Graben, and northwest-southeast-trending faults such as the Dunvegan and Tangent faults (Davies et al., 1997). Normal faults, including the Carboniferous to Permian Dawson Creek Graben Complex and precursor Precambrian basement normal and strike-slip faults, are abundant in the Peace River Embayment (PRE) (Barclay et al., 1990; Davies et al., 1997; Hope et al., 1999; Berger et al., 2008).

It has been seismically and structurally demonstrated that extensional normal faulting was episodically reactivated from the Devonian until the Cretaceous (Hope et al., 1999; Mei, 2009), particularly by loading of compressional thrust faults associated with the Jurassic Colombian and Cretaceous Laramide orogenies (O'Connell et al., 1990).

Diagenetic evolution and compositional modifications in the mineral assemblages of the Montney Formation occurred significantly from Early Triassic (early stage corresponding to shallow burial) to Late Cretaceous (Late stage corresponding to deep burial; Liseroudi et al., 2021; Vaisblat et al., 2017, 2021) and prior to maximum burial (80–60 Ma, Ness, 2001; Davies, et al., 1997; Ducros et al., 2017; Rohais et al., 2018). The Montney Formation has undergone uplift and erosion from the end of Paleocene to the present time (Ness, 2001; Ducros et al., 2017; Rohais et al., 2018). The Montney Formation entered the hydrocarbon generation window at approximately 90 Ma (Ness, 2001). The timing of maximum burial of the Montney Formation in British Columbia is estimated to be between 50–60 Ma (during the Laramide Orogeny) with a maximum burial temperature of approximately 160–170°C, adequate for thermogenic gas generation (Ness, 2001). This is evident from the increasing Montney thermal maturity trend to the west and southwest (Wood and Sanei, 2016; Gibbs and Rakhit, 2019; Euzen et al., 2021).

3 METHODS

3.1 Sample Material

Sixteen calcite-filled fracture samples were collected from a single core near the western margin of the Montney Formation in WCSB (**Figure 1**). Four doubly-polished thick section slides (100 μm thick) were prepared from the largest calcite fractures (**Figure 2**). This included two samples from the Lower Montney, one sample from the Middle Montney and one sample from the boundary of the Upper Montney and overlying Doig Formation (**Figure 1**). Vertical fractures were selected as opposed to horizontal fibrous "beef" calcite due to the small size of fluid inclusions in horizontal fracture calcite. Samples were prepared using a liquid cooled rotary saw to prevent modification of fluid inclusions.

3.2 Petrology and Fluid Inclusion Microthermometry

Fluid inclusion petrology followed the fluid inclusion assemblage (FIA) concept (Goldstein and Reynolds, 1994) to divide fluid inclusions into groups that were trapped contemporaneously. Detailed petrology was conducted on a Zeiss Axio Scope A1 Microscope fitted with a Linkam THMSG 600 Temperature control stage to heat to over 200°C and cool below –100°C. Petrographic images were captured with a Zeiss
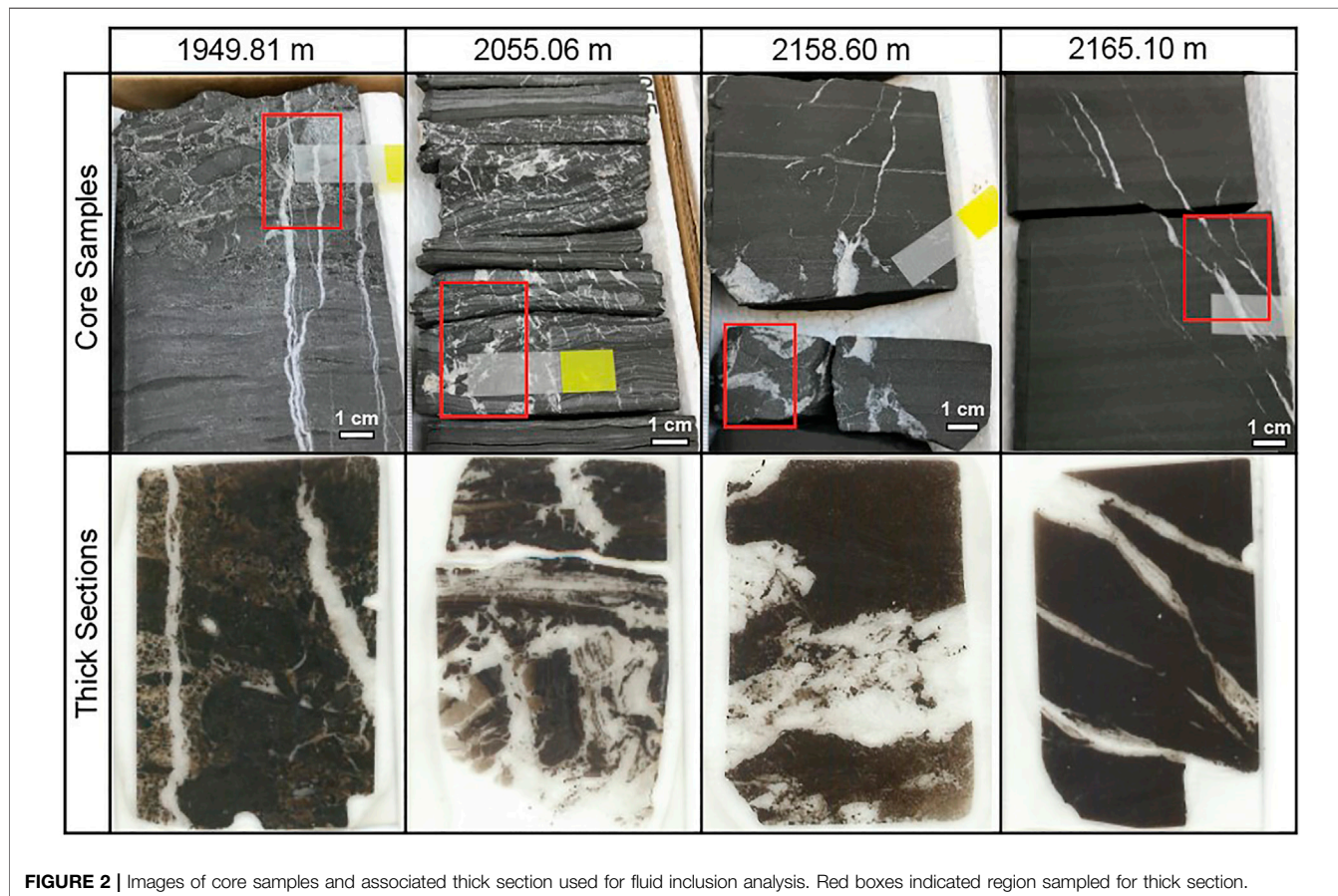
FIGURE 2 | Images of core samples and associated thick section used for fluid inclusion analysis. Red boxes indicated region sampled for thick section.

AxioCam ICc 5 camera using both white and ultraviolet light. Petrographic work was carried out at the Organic Petrology Laboratory, Geological Survey of Canada, Calgary. Calibration of this system was conducted using synthetic H_2O and CO_2 fluid inclusion standards for a precision of ± 1°C at 375°C and ± 0.2°C at −56.6°C. Homogenization temperatures were measured first to prevent stretching or decrepitation of fluid inclusions due to ice formation. Salinity was calculated from final ice melting temperatures (Tm) using the salinity-ice melt relationship of Bodnar (1993):

$$\text{Salinity (wt.\% NaCl)} = 1.78 \cdot (-\text{Tm}) - 0.0442 \cdot (\text{Tm}^2)$$
$$+ 0.000557 \cdot (\text{Tm3}).$$
$$(1)$$

Qualitative determination of the electrolyte composition in aqueous fluid inclusions was assessed by measuring the eutectic temperature (Te) when fluid inclusions devitrified following heating of frozen inclusion (Bodnar, 2003).

Isochore and bubble point curve calculations of aqueous fluid inclusions were modeled via the AqSo_NaCl program (Bakker, 2018) using measured homogenization and last ice melting temperatures. Petroleum phase envelopes and vapor fraction curves were calculated using the PVT simulation package PVTsim (Calsep Co.) using a recombined hydrocarbon composition derived from locally produced fluids (data from field operators). Isochore calculations for petroleum fluid inclusions were modeled using PVTsim software using petroleum fluid inclusion homogenization temperatures, petroleum vapour fraction (described in section 4.2), and the recombined hydrocarbon composition (method outlined in Aplin et al., 1999).

Fluorescence properties (i.e., λ_{max} and red/green quotient) were measured on a Zeiss Axio Imager A2M microscope equipped with an ultraviolet (UV) light source and the Diskus-Fossil system. 20 samples from various depths were measured using Hilgers fluorescence spectroscopy, measuring the full spectrum in the visible light range (400–700 nm); this method uses two filter cubes to measure intensity of fluorescence at 600 nm (red cube) and 520–570 nm (green cube).

3.3 Raman Spectroscopy

Gas and liquid fluid inclusions were analyzed using a Renishaw inVia Raman microscope equipped with a 1,200 line/mm grating, Leica ×100 objective (N.A. = 0.85), and a motorized stage. All spectra were collected in high confocality mode to restrict Raman analysis to the smallest possible volumes with a minimum spot size of 0.76 μm and focal length of 2 μm. Acquisition times varied between 5 and 60 s per accumulation and five accumulations were collected for each measurement. The system was aligned and calibrated daily using an internal silicon reference material. Excitation via a 532 nm green laser provided ~20 mW of power. Depth series analysis across fluid inclusions with a 1 μm step size (z-direction) was used to obtain the strongest Raman signal for fluid inclusion spectra. Renishaw Intelligent Background removal tool employing high order polynomial fitting was used to remove effects of fluorescence from calcite host

and/or hydrocarbons within the fluid inclusions. Raman spectra were collected at relative wavenumbers of between 100 and 3,100 cm^{-1}. All measurements were performed at room temperature (23°C).

The Raman peak position of methane varies as a function of pressure (Fabre and Couty, 1986; Hansen et al., 2001; Lin et al., 2007; Lu et al., 2007; Zhang et al., 2015). Therefore the pressure of methane inclusions can be calculated from the shift in the C–H stretching band, ν_1, by measuring the difference between ν_1 peak position in near ambient methane inclusions vs. high pressure inclusions using established relationships outlined in Lu et al. (2007) and Zhang et al. (2016). We created synthetic fluid inclusions at atmospheric pressure using fused silica capillary tubing similar to the method described by Chou et al. (2008). Briefly, a short length of deactivated fused silica tubing (0.32 mm OD) was cut and then the outer polymer coating removed before pure methane was loaded into the capillary, which was then capped using a small pieces of septa. The synthetic methane inclusions were used to calibrate the relationship between vapor pressure and methane C–H stretching Raman band position as detailed in Lu et al. (2007). A suite of three synthetic methane inclusions were analyzed giving an ambient pressure methane ν_1 peak position of 2,917 cm^{-1}.

3.4 Stable Isotope Analysis of Carbonates

Samples for carbonate isotope analysis were milled from calcite veins and host rock using a Sherline model 4,000 lathe equipped using either a 1 mm or 0.5 mm dental drill bit. All stable isotope analyses were conducted by the Isotope Science Lab at the University of Calgary. Carbonate isotope analysis was performed via CF-IRMS on a Thermo Finnigan GasBench coupled to a Delta V isotope ratio mass spectrometer. Samples are weighed into Labco Exetainers capped and flushed with helium and then heated to 25°C at which point they were reacted with anhydrous phosphoric acid for >5hrs. CO_2 in the headspace is then sampled and analyzed six times per sample. Samples are corrected for instrumental effects using a suite of internal lab standards and normalized to VPDB using NBS-19. Values are reported in standard delta (δ) notation in ‰ VPDB, with oxygen isotope values converted to VSMOW scale (for water modeling) using the equation (Brand et al., 2014):
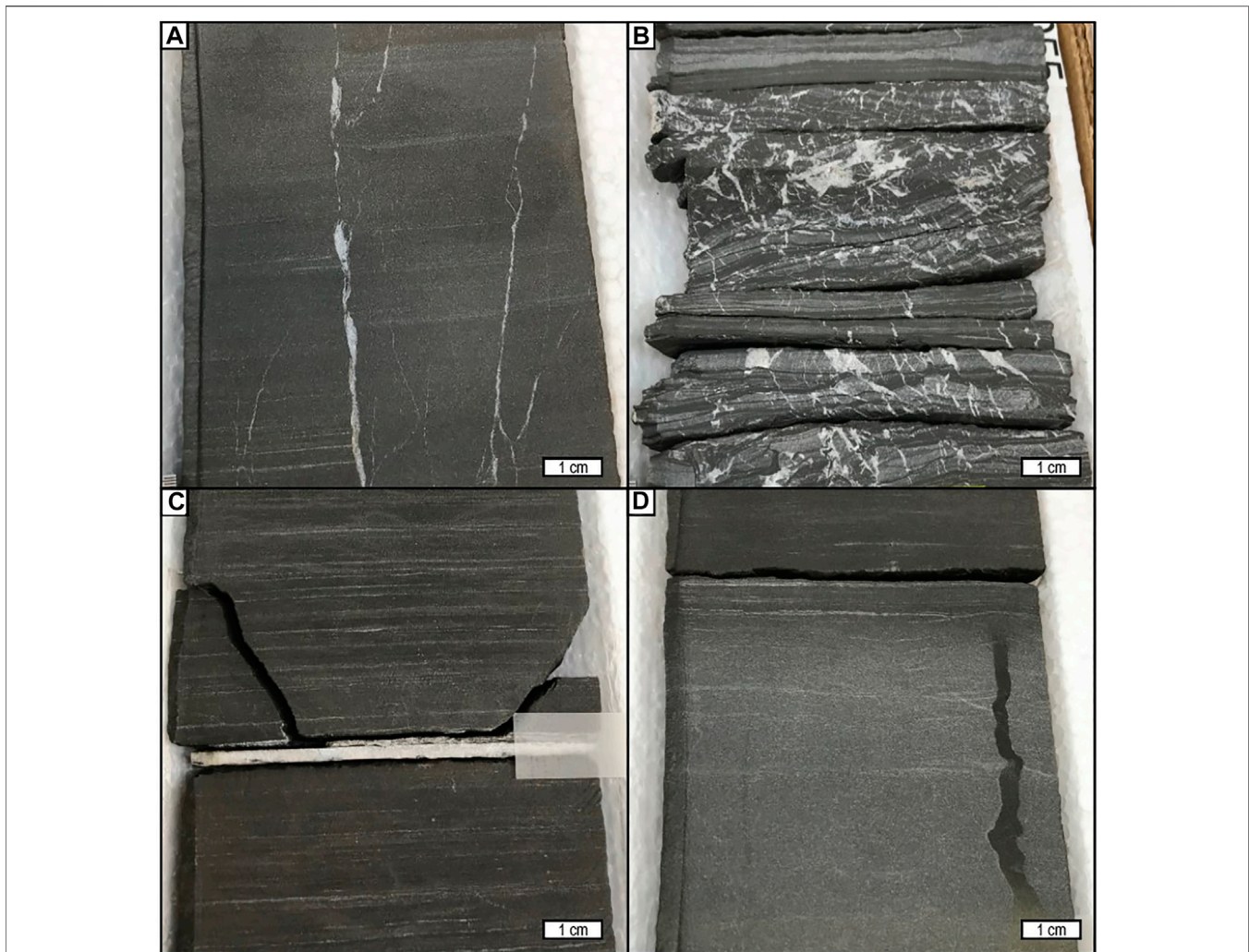
$$\delta^{18}O_{VPDB} = 0.97001 \times \delta^{18}O_{SMOW} - 29.99‰. \quad (2)$$

Dolomite samples (host rock) were $\delta^{18}O$-corrected using the dolomite fractionation factor calculated after Rosenbaum and Sheppard (1986).

4 RESULTS

4.1 Fractures

Four types of fractures were observed in the core: 1) vertical to sub-vertical calcite-filled fractures with blocky calcite textures

FIGURE 3 | Fracture types. **(A)** Vertical fractures. **(B)** Brecciated zone. **(C)** Bedding-plane parallel fracture. **(D)** sediment-filled fractures rich in organic matter.

(**Figure 3A**, **Figure 4A**); 2) highly fractured brecciated zones with a combination of vertical and horizontal fractures with a mostly blocky calcite texture (**Figure 3B**); 3) horizontal bedding plane parallel fractures (beefs) composed of calcite with complex fibrous and blocky textures (**Figure 3C**); and 4) sediment-filled fractures rich in organic matter (**Figure 3D**). Vertical to sub-vertical fractures are generally ≤10 mm wide, greater than 10 cm in length, but exhibit minimal vertical displacement (<10 mm) and are likely tensile fractures related to hydraulic fracturing. Bedding-plane parallel fractures are ≤10 mm thick and thought to extend over significant horizontal distances (D. Laycock, pers. comm.). Horizontal and brecciated fractures display more complex textures with evidence of multiple crack-seal episodes similar to that reported by Gasparrini et al. (2021). Vertical fractures have secondary fluid inclusions in healed fractures (see below), which when combined with complex textures in the horizontal and brecciated fractures indicates fractures have experienced multiple fluid flow and precipitation events.

4.2 Fluid Inclusions

Fluid inclusions are abundant within the calcite-filled fractures of all four samples and consist of a complex mixture of aqueous, petroleum, and gas-rich inclusions. Aqueous fluid inclusions were observed in all samples, although were rare (n = 3) in the brecciated sample (2055 m) despite the presence of abundant petroleum inclusions. Petroleum fluid inclusions were also observed in all samples, however, were rare (n = 3) in the deepest sample (2,165 m).

Primary two-phase, liquid-vapour (LV), aqueous fluid inclusions typically occur as groups of large negative-crystal shaped inclusions oriented along the axis of crystal growth (**Figure 4B**). These inclusions are generally isolated, do not occur in assemblages along fracture planes, and do not occur within the same fluid inclusion assemblages as petroleum inclusions (**Figures 4C,D**). In addition, the absence of mixed inclusions (aqueous inclusions that contain an immiscible petroleum phase) indicates that aqueous and petroleum inclusions are not coeval. Aqueous fluid
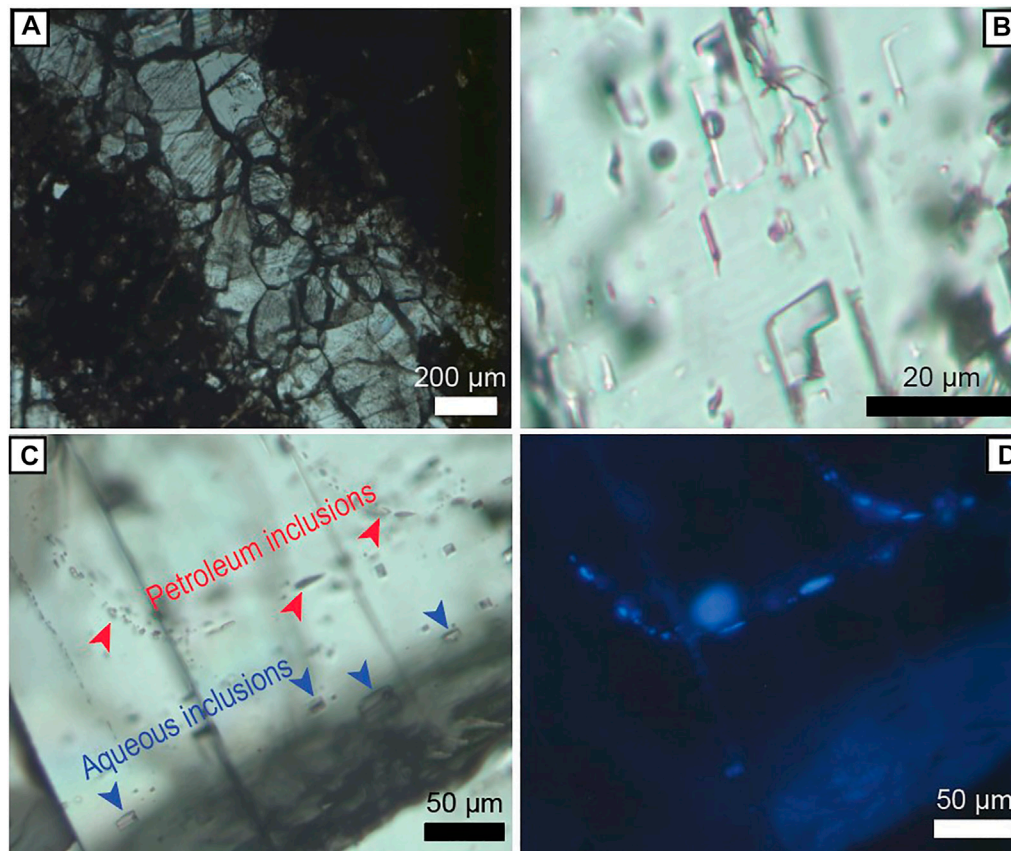
FIGURE 4 | Fluid inclusion photomicrographs. **(A)** Blocky calcite texture typical of calcite veins used in this study. **(B)** Aqueous fluid inclusions with negative crystal shape (2,165 m). **(C)** Primary aqueous fluid inclusions and secondary petroleum inclusion assemblage (1949 m). **(D)** Same as **(C)** but UV illumination showing fluorescing petroleum and non-fluorescing aqueous inclusions.

inclusions are also typically larger than petroleum inclusions, have lower vapor fractions (detailed below), and do not exhibit fluorescence under UV illumination.

Two-phase liquid-rich petroleum fluid inclusions in the vertically oriented fracture samples (i.e., 1949 m, 2158 m, and 2,165 m) are generally irregular or ellipsoidal-shaped, and dominantly occur as secondary inclusion assemblages along cleavage planes (**Figures 5A,B**) or along sinuous paths (**Figures 5C,D**). The brecciated fracture sample (2055 m) is dominated by abundant petroleum inclusions. This includes evidence for inclusions derived from the maturation of organic matter in the host rock (**Figures 5E,F**) and as clouds of inclusions within the cores of calcite crystals (**Figures 5G,H**) suggesting a primary origin. Primary petroleum inclusions are only observed in the brecciated sample, whereas in all other samples petroleum inclusions are classified as secondary.

Single-phase gas inclusions are generally ellipsoidal in shape, non-fluorescing, often occur within petroleum fluid inclusion assemblages, and are composed of methane with minor contribution of other light hydrocarbons (see section 4.3). In addition, solid bitumen inclusions occur in the form of irregular shaped masses either along petroleum fluid inclusion assemblages or isolated with crystals centers. All petroleum fluid inclusions

exhibited a consistent blue-white fluorescence color (maximal intensity wavelength of 452 nm ±1 nm) under UV illumination (**Figure 4D**; **Figures 5B,D,F,H**)

Microthermometric measurements were made on aqueous inclusions and petroleum-bearing inclusion, which includes homogenization temperatures (Th) from both aqueous and petroleum inclusions and ice melting temperatures (Tm) from aqueous inclusions as petroleum inclusions did not freeze at temperatures as low as –100°C. Eutectic temperatures (Te) were measured on several aqueous fluid inclusions to assess fluid electrolyte composition. All microthermometry results are presented in **Table 1** and **Figure 6**. Homogenization temperatures for aqueous fluid inclusions ranged from 93°C to 149°C with a mean value of 124 ± 12°C (n = 70), and a median value of 124°C. The Th of petroleum-bearing fluid inclusions ranged from 36°C to 87°C with a mean value of 48 ± 9°C (n = 67), median value of 46°C. However, 80% of the petroleum-bearing inclusions have Th values between 40 and 50°C. There is no significant difference in Th values as a function of depth for either aqueous or petroleum-bearing fluid inclusions. The observed homogenization temperatures for both aqueous and petroleum fluid inclusions are slightly higher than the mean values reported by Gasparrini et al. (2021) for another Montney well (aqueous = 100°C; petroleum = 31°C), but both datasets have a
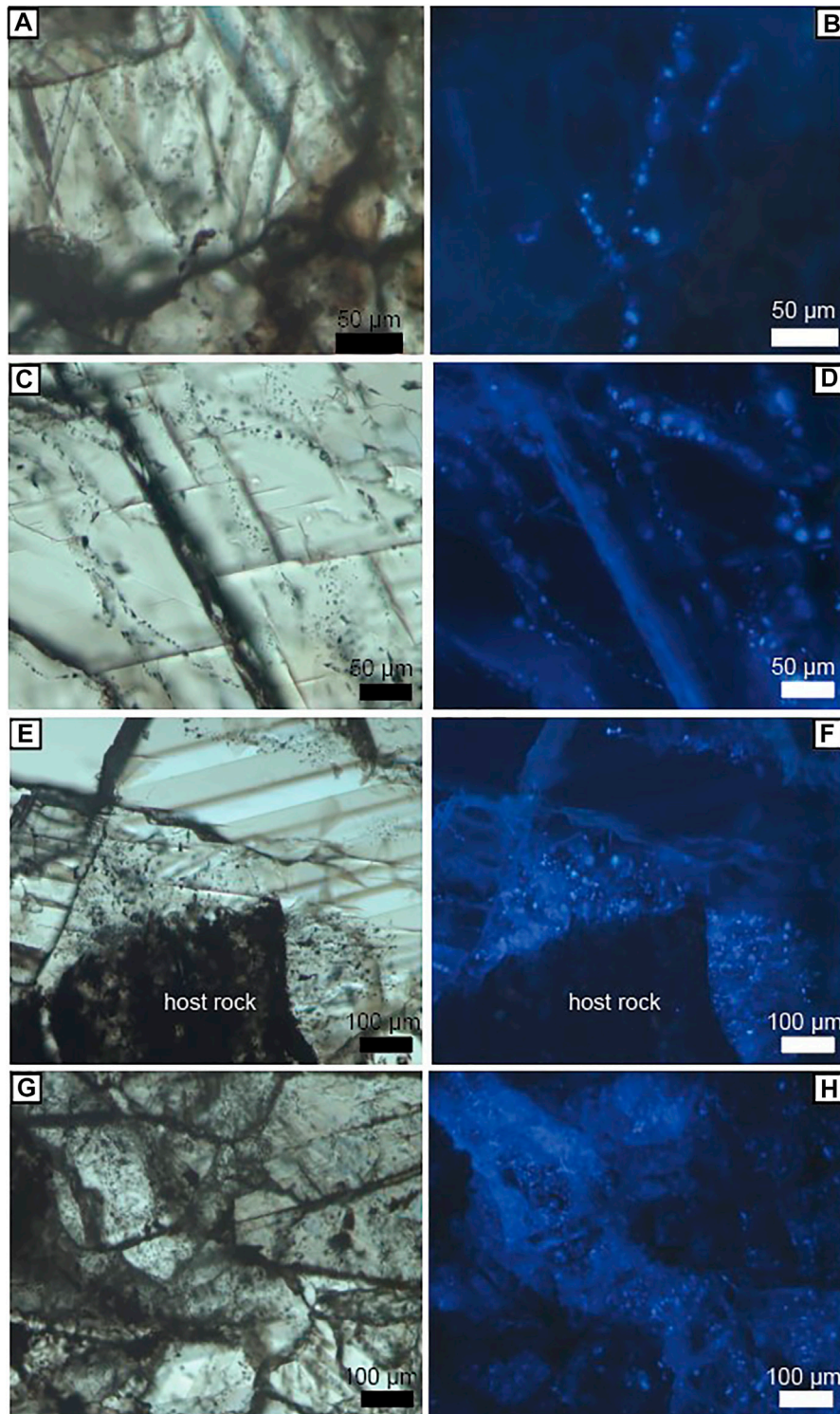
FIGURE 5 | Petroleum fluid inclusion photomicrographs. **(A)** Secondary bi-phase petroleum inclusions forming along cleavage planes. **(B)** Same as field of view (FOV) as previous under UV illumination showing fluorescing petroleum inclusions. **(C)** Healed fractures in calcite vein with sinous paths of secondary bi-phase petroleum inclusions (2055 m). **(D)** Same FOV as previous under UV illumination. **(E)** Primary bi-phase petroleum inclusions from brecciated zone (2055 m) displaying maturation of organic matter from host rock and exsolving petroleum fluids. **(F)** Same FOV as previous under UV illumination. **(G)** Blocky calcite from brecciated zone (2055 m) with clouds of primary bi-phase petroleum inclusions within the cores of vein calcite crystals. **(H)** Same FOV as previous under UV illumination.

TABLE 1 | Fluid inclusion microthermometry results.

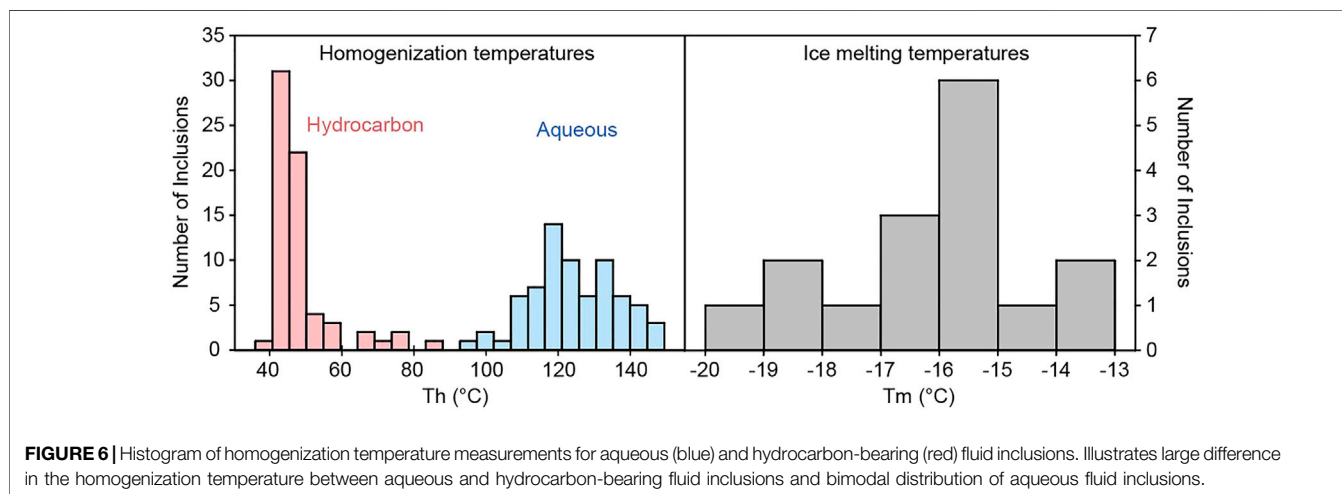| Depth		Aqueous fluid inclusions				HC-bearing	
(m)		Th (°C)	Tm (°C)	Salinity (%)	Te (°C)		Th (°C)
1949.81	n	23	7	7	1	n	17
	Avg	119.7	-15.4	18.9	-51.0	Avg	49.0
	SD	10.8	1.6	1.3	-	SD	7.5
	Max	141.4	-13.4	21.0	-51.0	Max	73.3
	Min	92.9	-18.1	17.3	-51.0	Min	41.2
2055.06	n	3	0	0	0	n	39
	Avg	129.6	-	-	-	Avg	49.3
	SD	20.3	-	-	-	SD	11.1
	Max	149.4	-	-	-	Max	87.2
	Min	108.8	-	-	-	Min	36.0
2,158.6	n	21	4	4	2	n	9
	Avg	131.8	-17.3	20.4	-52.0	Avg	45.1
	SD	9.1	1.8	1.3	0.1	SD	1.6
	Max	145.1	-16.0	22.4	-51.9	Max	47.9
	Min	107.8	-20.0	19.4	-52.0	Min	43.1
2,165.1	n	22	4	4	4	n	3
	Avg	119.7	-16.0	19.4	-51.0	Avg	44.0
	SD	11.4	1.3	1.0	1.4	SD	1.8
	Max	141.2	-15.1	21.0	-50.0	Max	45.8
	Min	98.0	-18.0	18.7	-53.0	Min	42.2

consistent difference between measured Th in aqueous and petroleum fluid inclusions.
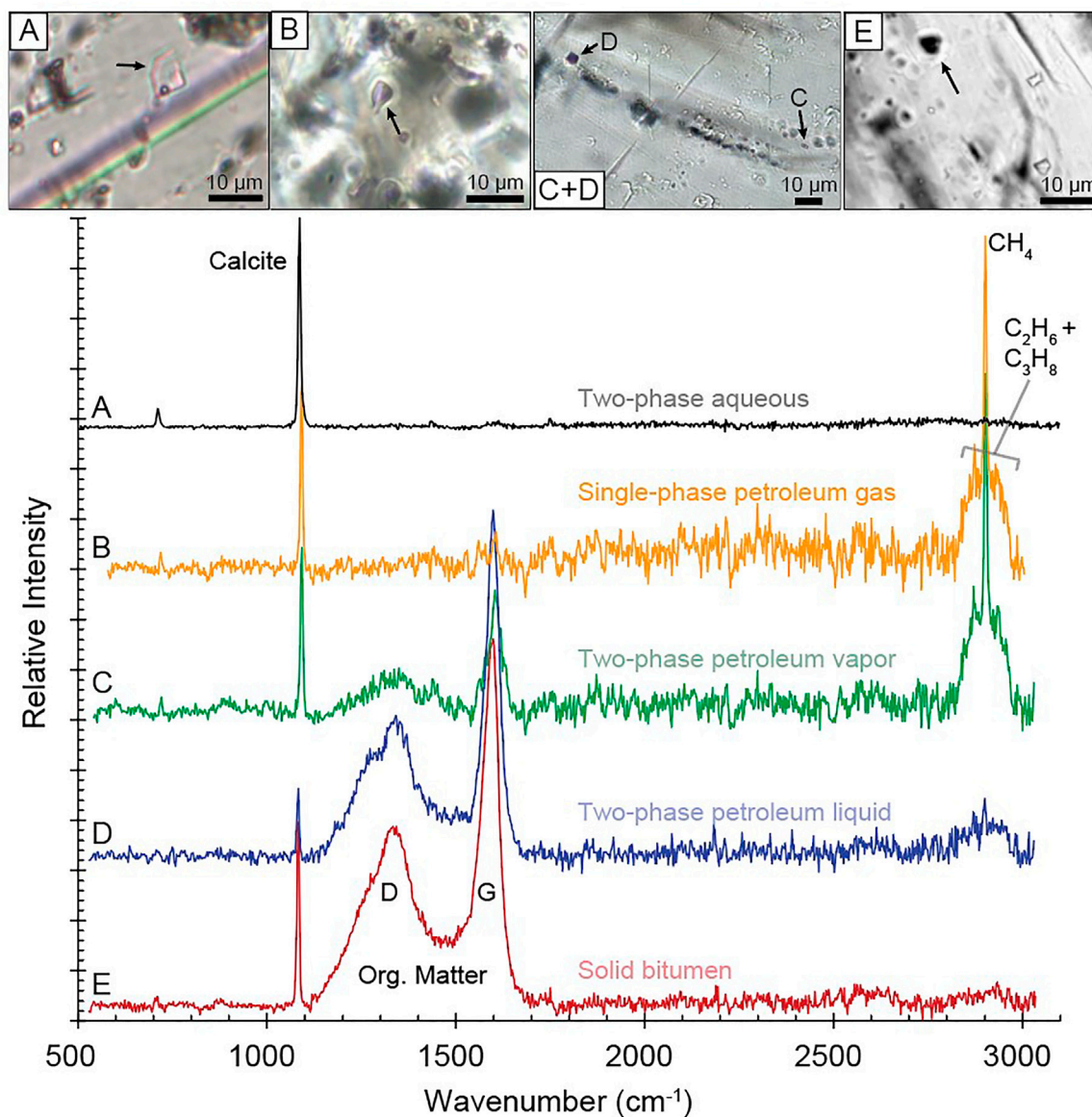
Ice-melting temperatures (Tm) for aqueous fluid inclusions ranged from −20.0°C to −13.5°C with a mean value of −16.5 ± 2.1°C (n = 11) and exhibit minimal variability with depth (**Figure 6**). These ice-melting temperatures correspond to fluid salinities of between 17.3 and 22.4 wt% equivalent NaCl, with an average salinity of 19.6 wt% NaCl equivalent. These values are nearly identical to those reported by Gasparrini et al. (2021), suggesting similar fluids were responsible for the calcite cementation at both locations. Eutectic temperatures for aqueous inclusions ranged from −53°C to −50°C (n = 7). These low eutectic temperatures are consistent with the presence of Ca^{2+} or other divalent cations along with NaCl and suggests a $NaCl-CaCl_2$ brine composition (Bodnar, 2003).

Measurements of the vapor fraction in fluid inclusions were made using the Zeiss Zen® Software area calculations. These are 2D measurements that are unable to account for depth and therefore have a higher degree of uncertainty. Measurement of a suite of 54 fluid inclusions indicates the average vapor fraction in aqueous inclusions is 0.045 (σ = 0.009) compared to petroleum inclusions that averaged 0.21 (σ = 0.073) vapor. Isochore-based calculations for the average aqueous inclusion molar volume (19.23 cm^3mol^{-1}) yields a fraction of vapor equal to 0.051 at 25°C, lending confidence to the accuracy of 2D vapor fraction measurements. The average petroleum inclusion vapor fraction measurement (0.21) is used in isochore modeling.

4.3 Raman Spectroscopy

All Raman spectra from fluid inclusions had significant fluorescence from the calcite host and from hydrocarbons within inclusions. Fluorescence effects were removed from Raman spectra by subtracting a polynomial curve fit to the baseline. The Raman spectra of the different fluid inclusion types are shown in **Figure 7**. Two phase aqueous LV fluid inclusions (**Figure 7A**) have strong calcite bands from the host and no evidence of other gases such as methane or other hydrocarbons. This suggests hydrocarbons were either not present during the formation of aqueous inclusions, or immiscible; in either case the lack of CH_4 in the aqueous inclusions indicates the H2O+ NaCl (or the H2O+ NaCl + $CaCl_2$) system can be used to model aqueous inclusion trapping conditions (e.g., Chen at al., 2016). Single-phase petroleum gas inclusions (**Figure 7B**) are non-fluorescing and exhibit strong methane C–H stretching bands (v_1) at 2,905 cm^{-1}, smaller peaks at 2,954 and 2,890 cm^{-1} surround the C–H stretching peak and are interpreted as ethane or other light hydrocarbons (cf. Frezzotti et al., 2012), and strong calcite signals from the host mineral. Similar to gas-rich inclusions, vapor in two-phase petroleum inclusions (**Figure 7C**) display strong Raman signals in the light-hydrocarbon gas region (2,300–3,000 cm^{-1}) as well as calcite bands (712 and 1,085 cm^{-1}) and two broad bands from organic matter in the disordered (D) and graphite (G) band regions located at c. 1,350 cm^{-1} and c. 1,580 cm^{-1}, respectively (c.f. Henry et al., 2019). Two-phase petroleum liquids (**Figure 7D**) have strong Raman signals in the organic matter D- and

FIGURE 6 | Histogram of homogenization temperature measurements for aqueous (blue) and hydrocarbon-bearing (red) fluid inclusions. Illustrates large difference in the homogenization temperature between aqueous and hydrocarbon-bearing fluid inclusions and bimodal distribution of aqueous fluid inclusions.

FIGURE 7 | Raman spectra of fluid inclusions, note that fluorescence background has been subtracted from all spectra. **(A)**. Two-phase aqueous fluid inclusions showing strong calcite peaks associated with host material and an absence of hydrocarbons. **(B)**. Single-phase petroleum gas fluid inclusion showing strong methane band and associated hydrocarbon gases (e.g., ethane, propane, etc.). **(C)**. Two-phase petroleum vapour from vapour bubble showing large methane band and organic matter D- and G-bands. **(D)**. Two-phase petroleum liquid fluid inclusions with strong D- and G-bands and weak methane band. **(E)**. Solid bitumen inclusions showing typical D- and G-band organic matter peaks.

G-bands and reduced light hydrocarbon gas signals. Finally, solid bitumen inclusions (**Figure 8E**) in calcite have very strong (and narrower) D- and G-bands, and light hydrocarbons gas are absent. No other typical non-hydrocarbon gases (e.g., CO_2 and H_2S) were detected in either the aqueous or petroleum inclusions.

4.4 Stable Isotope Geochemistry (δ^{13}C and δ^{18}O)

Stable isotope values from vertical and horizontal fracture calcite are shown alongside similar data from Gasparrini et al. (2021) (**Figure 8**). The carbon isotope composition of fracture-filling calcite ranges from –7.3‰ to +3.8‰ (mean of –2.6‰) and the oxygen isotope composition varies from –10.2‰ to –6.1‰ (mean of –9.0‰). One sample of a shell fragment has a δ^{13}C value of –5.1‰ and δ^{18}O value of –0.4‰, which is within the bounds of equilibrium with Early Triassic seawater (Veizer et al., 1999). The large difference in δ^{18}O values between the shell fragment and fracture filling calcite combined with an agreement with Triassic seawater indicates there was not wholesale re-equilibrium of carbonates. Also, there is an apparent lack of exchange between host rock

carbonates (both dolomite and fracture filling calcite) and bioclastic carbonate material.

The $\delta^{18}O$ values of vertical fracture calcite is similar to bulk-rock dolomite $\delta^{18}O$ values for a given depth (see red vs. yellow datapoints in **Figure 9**) ranging from –9.9‰ to –6.6‰. The $\delta^{13}C$ values of calcite from vertical fractures vary from –7.3‰ in the Upper Montney/Doig Formation to –1.2‰ in the Lower Montney. This +6.1‰ shift in $\delta^{13}C$ values with depth is associated with a +5.2‰ shift in mud-gas methane values from –49.2‰ to –44.0‰ (**Figure 9**). The $\delta^{18}O$ values of calcite from bedding plane parallel fractures have a narrow range in values (blue in **Figure 8**). The $\delta^{18}O_{H2O}$ values of pore water are also plotted, alongside fracture calcite $\delta^{18}O_{carb}$ values (**Figure 9**).

5 DISCUSSION

## 5.1 Fluid Inclusions Isochore Modeling and Timing of Fracture Formation

Characterization of aqueous and petroleum fluid inclusions helps elucidate the physical and chemical conditions during trapping and provides a record of hydrocarbon maturation and migration within the Montney Formation. The 56°C range in homogenization temperatures from aqueous inclusions may

indicate multiple generations of fluid flow, however the discrimination of these events is not readily discernable from the studied samples, and therefore they are categorized as a single generation. Petroleum inclusions occur as both primary inclusions (e.g., in the brecciated sample, 2055 m, **Figures 5E–H**) and as secondary assemblages within the vertical calcite-filled fractures that host the primary aqueous fluid inclusions (**Figures 5A–D**). Despite occurring as primary and secondary assemblages, petroleum inclusions exhibit a narrow range in physio-chemical characteristics (e.g., homogenization temperatures, vapor fractions, fluorescence color, Raman band shifts) implying similar pressure-temperature conditions and fluid composition during entrapment. Limited range in fluorescence color may indicate either a single generation of hydrocarbons (Munz, 2001) or post-depositional alteration via phase separation or gas/water washing (Bourdet et al., 2014), however there is no evidence of gas/water washing. Low variance in the vapour-liquid ratio of petroleum fluid inclusions indicates homogeneous entrapment (Rongxi et al., 2011). This evidence strongly suggests a single generation of petroleum inclusions within these samples.

Aqueous and petroleum inclusions were not observed in the same fluid inclusion assemblages. Raman spectroscopy analysis reveals hydrocarbons are absent from aqueous inclusions, which would be expected as the presence of methane or other water-
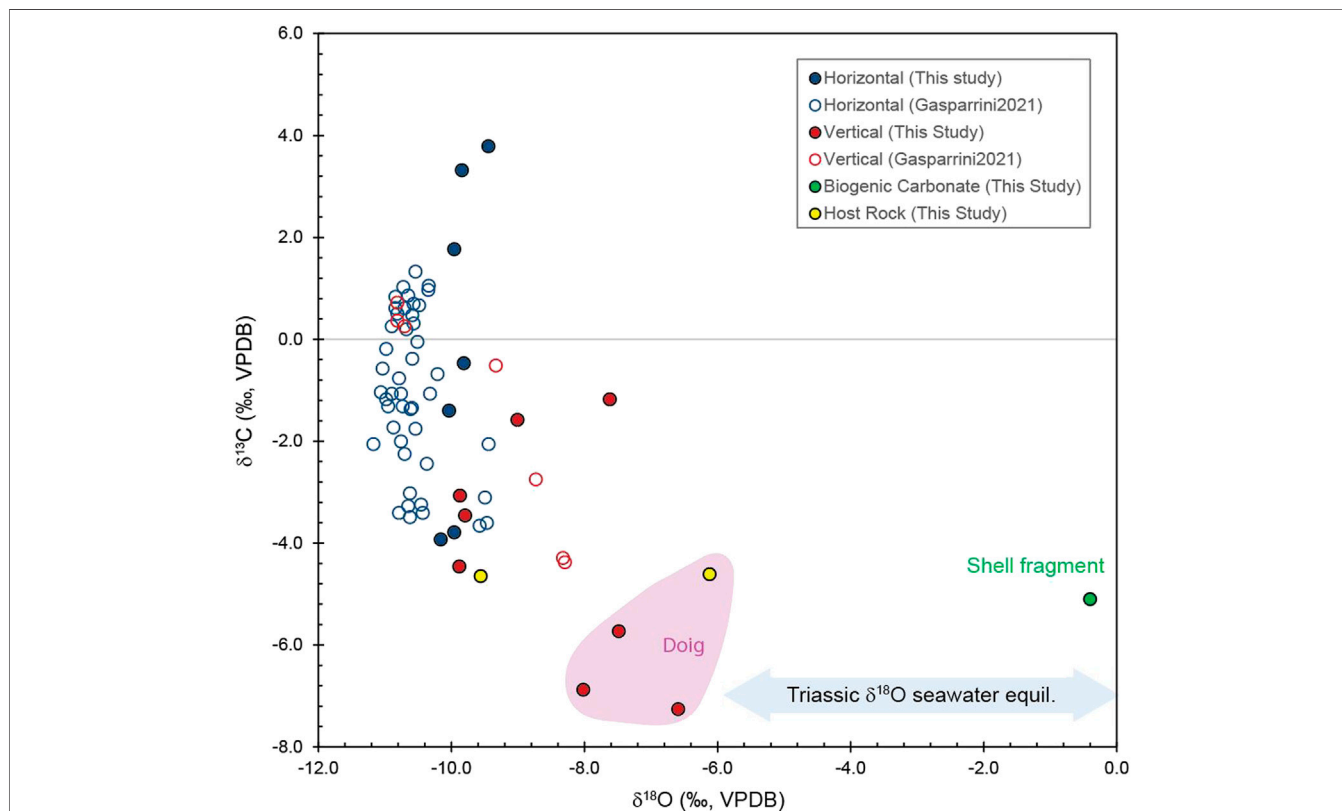
FIGURE 8 | Crossplot of $\delta^{13}C$ and $\delta^{18}O$ from stable isotope analysis of different carbonate phases. Fracture calcite data from this study and Gasparrini et al., (2021). Biogenic carbonate (shell fragment) plots close to predicted Triassic seawater $\delta^{18}O$ values. Vertical and horizontal (bedding-plane parallel) fracture calcite and host rock dolomite exhibit $\delta^{18}O$ values 6–10‰ lower then predicted if derived from Triassic seawater.
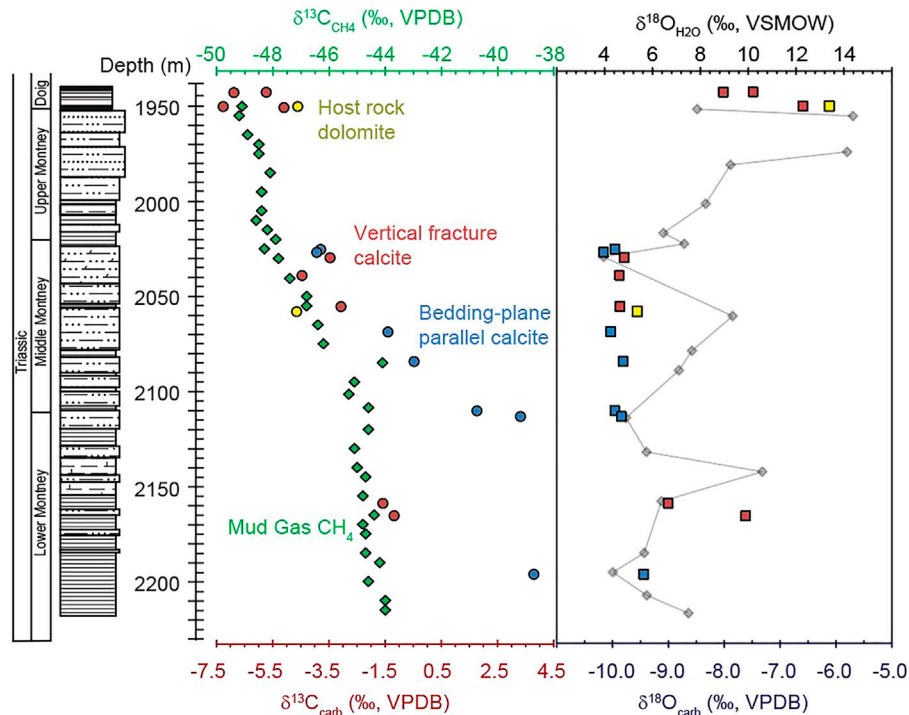
FIGURE 9 | Downhole variability in δ¹³C values of vertical fracture calcite (red circles), horizontal bedding-plane parallel fracture calcite (blue circles), host rock dolomite (yellow circles), and methane derived from mud-gas during drilling (green diamonds). All carbonate values (vertical and horizontal bedding-plane parallel calcite) are plotted along bottom scale, and mud-gas CH₄ is plotted along top scale. Note the magnitude of δ¹³C scales for methane and carbonates are equivalent, but different values. δ¹⁸O values of fracture calcite (red and green boxes) plotted alongside δ¹⁸O of pore water (grey diamonds). Stratigraphy adapted from Laycock et al. (2021).
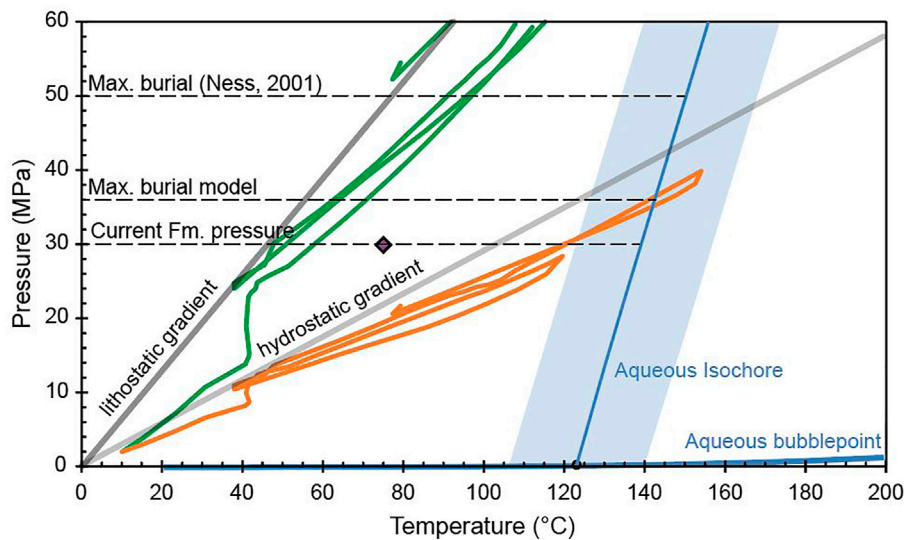
FIGURE 10 | Pressure-temperature modeling for aqueous fluid inclusions. Aqueous bubblepoint curve calculated based on a measured salinity of 19.6% NaCl equiv. using the Aq_NaCl program (Bakker, 2018). Average aqueous isochore shown as dark blue line with minimum and maximum measured Th + Tm values defining light blue envelope, all values calculated using Aq_NaCl program. Green and orange lines are lithostatic and hydrostatic gradients respectively, derived from a burial history model for this well (**Figure 11**). Grey lithostatic and hydrostatic gradients calculated using a depth-pressure gradient of 10.18 kPa/m and a local geothermal gradient of 35°C/km (Weides and Majorowicz, 2014) based on modern conditions. Maximum burial pressure from two different burial history models are shown as grey dashed in, see text for details.
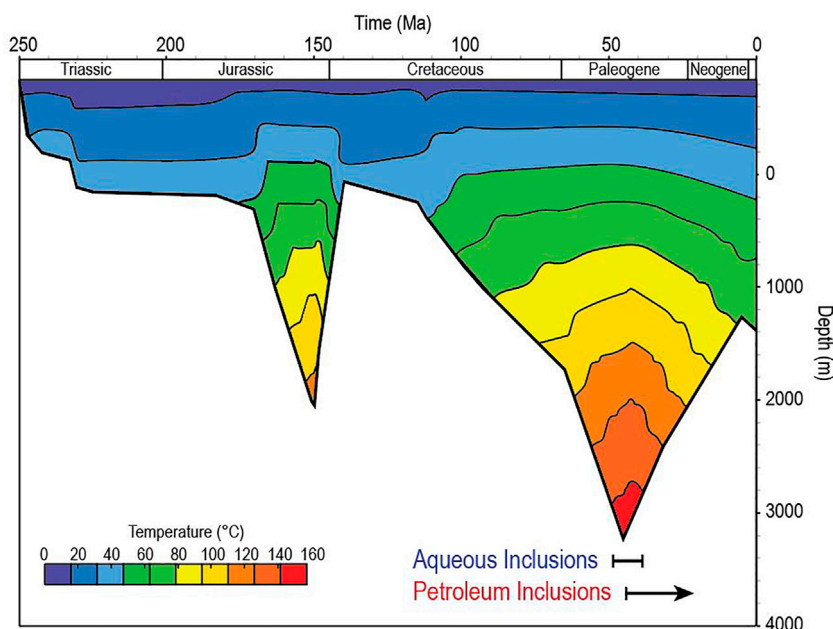
FIGURE 11 | Burial and thermal history for this well. Data derived from the British Columbia Oil and Gas Commission data archives. Estimated timing for entrapment of aqueous and petroleum inclusions shown occurring during the Laramide Orogeny ~50 Ma.

soluble organic compounds (e.g., benzene and toluene) typically occur due to interactions between water and oil in the basin (*cf.* Ruble et al., 1998; Gao et al., 2017). Finally, the intersection of the modeled petroleum and aqueous inclusion isochores is in excess of the pressure-temperature conditions expected for this system. Therefore, we conclude that aqueous and petroleum inclusions are not co-genetic and require separate PVT modelling.

5.1.1 Aqueous System

Aqueous fluid inclusion isochore and bubble point data is plotted alongside hydrostatic and lithostatic gradients based on modern geothermal gradients (35°C/km, Weides and Majorowicz, 2014) and a depth-pressure gradient of 10.18 kPa/m (**Figure 10**). Modern measured reservoir pressure is between the hydrostatic and lithostatic gradient, indicating overpressure conditions currently exist within the reservoir. Also plotted are burial-history based lithostatic and hydrostatic conditions for the well, which generally agree with those calculated from the modern conditions described above. The aqueous isochore intersects with the modern formation pressure at 140°C, however this is below the hydrostatic gradient and would indicate underpressure conditions, which is unlikely. The intersection of the aqueous isochore with the hydrostatic gradient indicates a minimum trapping temperature of ~142°C (i.e., ≥18°C pressure correction).

Burial history for this well was derived from depositional age models and vitrinite reflectance measurements (**Figure 11**) and indicates that maximum burial depths and temperatures occurred during the Laramide orogeny at ~50 Ma (Watt et al., 2022; this study). Modeled trapping temperatures of ~142°C indicate fracture-filling calcite formation during peak burial,

as formation temperatures greater than 140°C only developed during this period. Therefore, we suggest that the vertical fractures must have formed during peak burial, associated with the Laramide orogeny, and are therefore a late-diagenetic feature. Burial history models for other Montney wells, including those of Ness (2001) and Ducross et al. (2017), show deeper burial during the Laramide orogeny, potentially up to 5 km. This extends the timeframe during which formation temperatures >140°C were present, however all models indicate that the Laramide is the only event resulting in burial in excess of the 2 km that is required to produce the trapping temperatures measured in aqueous fluid inclusions. Timing of entrapment reported by Gasparrini et al. (2021) occurs prior to peak Laramide burial because their measured Th values and pressure corrections to aqueous inclusions were lower than peak burial temperatures predicted by the burial model. However, owing to the higher trapping temperatures measured in this core, initial fracture formation and calcite precipitation is suggested to occur during peak burial at approximately 50 Ma.

Eutectic and last ice melting temperatures indicate fluids with a 19 wt% NaCl-CaCl$_2$ brine composition, similar to those measured in aqueous fluid inclusions from Devonian and Mississippian calcite and dolomite cements (Adam, 2000; Al-Aasm and Clarke, 2004; Rivas, 2004; Davies and Smith, 2006; Al-Aasm et al., 2019). Devonian formation waters are generally composed of high-salinity calcium chloride brines, which may be the result of brine interactions with Precambrian basement rocks (Spencer, 1987). This may imply previous connectivity between these systems, however, the fluids must have been in place prior to the development of the low-permeability conditions
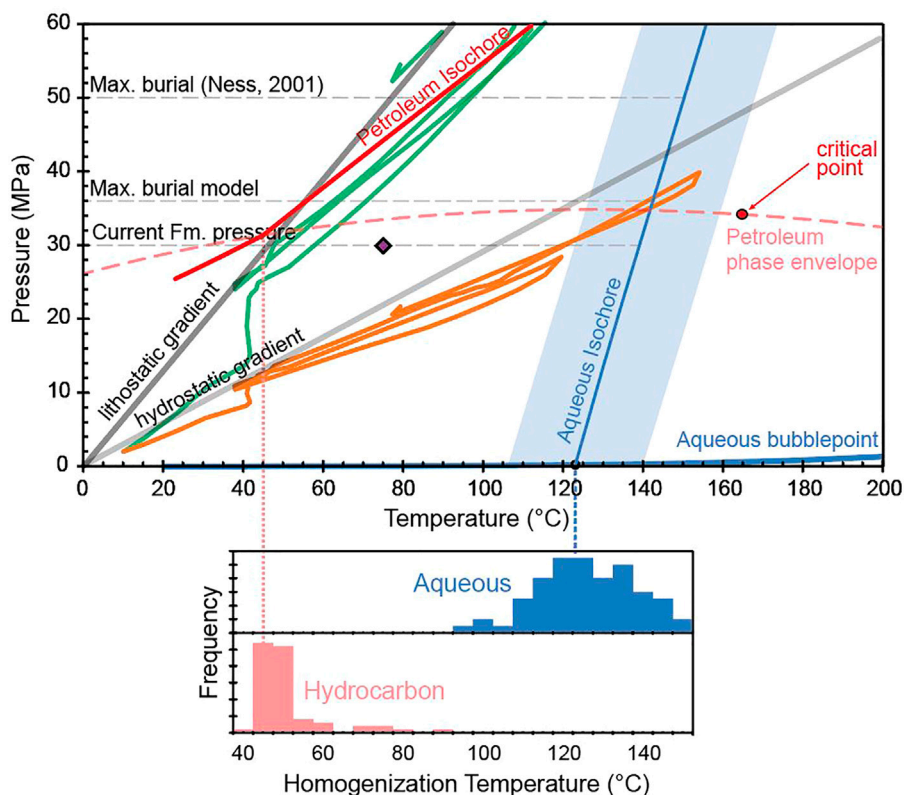
FIGURE 12 | Pressure-temperature modeling for petroleum fluid inclusions shown alongside aqueous isochore. Note that aqueous and hydrocarbon inclusions are not coeval. Phase envelope calculated using PVTsim (Calsep Co.) from locally derived recombined hydrocarbon fluid composition (red dashed line). Current formation pressure shown as purple diamond. Petroleum inclusion isochores (red solid line) calculated using an average homogenization temperature of 45°C and petroleum fluid compositions from recombined Montney fluids.

that were present during the formation of these fractures, discussed further below.

5.1.2 Petroleum System

Pressure-temperature modelling of petroleum inclusions is plotted alongside the calculated phase envelope for petroleum fluids (**Figure 12**). It should be noted that the phase envelope and petroleum isochore was calculated using recombined petroleum fluid compositions derived from modern produced fluids (data from operator). Therefore, it is possible that the composition of modern produced fluids is different from that within the studied petroleum fluid inclusions. However, due to the low permeability of the Montney Formation (Ghanizadeh et al., 2015), current state of overpressure conditions, and the lack direct measurement of fluid inclusion composition, we assume that the modern recombined fluid composition is reflective of the fluids within the petroleum inclusions. In addition, the PVTsim (Calsep Co.) software has been shown to produce reliable models provided the petroleum composition is at least genetically related (i.e., from the same region) to the inclusion composition (Aplin et al., 1999).

The most striking feature of this modeling is the proximity of the petroleum isochore to the lithostatic gradient. Entrapment of petroleum inclusions near the lithostatic gradient indicates fluids sourced from a high-pressure system. We infer that the

development of overpressure caused by hydrocarbon degradation and thermal cracking during peak burial resulted in the formation of brecciated horizons and the reactivation of previous (vertical) fracture systems. As evidenced by primary petroleum inclusions within the brecciated horizon exsolving from the host rock (**Figures 5E–H**) and secondary petroleum inclusions trapped in healed fractures within the vertical fractures (**Figures 5A–D**).

Furthermore, the formation of bedding-plane parallel fractures (beefs) has been shown to be associated with overpressure conditions (Rodrigues et al., 2009; Cobbold et al., 2013; Zanella et al., 2021). Beefs in shale-siltstones beds form via the development of overpressure, when pore fluid pressure exceeds lithostatic pressure at a specific depth (Cobbold et al., 2013), related to mechanical compaction (e.g., crustal shortening) and/or hydrocarbon generation/degradation (Zanella et al., 2021). The abundance of beefs in this core supports the interpretation that overpressure developed near or in excess of the lithostatic pressure and implies near synchronous formation of beef and brecciated horizons.

5.1.3 Raman Spectroscopy

Similarities in the Raman methane v_1 peak position between all petroleum inclusions (**Figures 7B–D**) indicates these inclusions

were trapped under similar pressure-temperature conditions. Indeed, the similarities in vapor fractions in petroleum fluid inclusions, the monochromatic fluorescence of these inclusions, and low variance in homogenization temperatures all suggest near synchronous formation of all petroleum inclusions independent of any depth related changes in thermal maturity.

Raman spectroscopy of petroleum inclusions reveals bathochromic downshifts to the methane C–H stretching band, ν_1, in both single-phase gas and two-phase petroleum inclusions, which indicates high pressure or high methane densities (Lin et al., 2007; Burruss et al., 2012). According to Hansen et al. (2001) who measured shifts in the methane ν_1 Raman band in methane-ethane mixtures at different pressures, there is a weakening of the C-H bond, which is intensified in methane-ethane mixtures with increasing ethane contents (and would be presumably also enhanced by the presence of other hydrocarbons). This weakening of the bond caused in part by enhanced van der Waals interactions leads to charge redistribution resulting in a stronger pressure dependence on the methane ν_1 band position peak (Hansen et al., 2001). The observed methane band position in this study at 2,905 cm^{-1} is consistent between all measured gas and petroleum inclusions and thus independent of the relative proportions of liquid and vapor (e.g., single-phase gas and two-phase) in the inclusion. This suggests that either vapor composition is the same in all fluid inclusions, or that this enhanced charge redistribution has a limit, similar to the lower limits of the pressure-methane ν_1 band position relationship shown for pure methane (Fabre and Couty, 1986; Lin et al., 2005; Lu et al., 2007; Zhang et al., 2016). Notably, the methane ν_1 band position of 2,905 cm^{-1} is consistent with methane band positions for gas hydrates (large cavity CH$_4$), and indeed we also observe the smaller 2,914 cm^{-1} band (small cavity CH$_4$) typically observed in methane hydrates (e.g., Sum et al., 1997). The origin of this gas hydrate-like signature is unknown.

5.2 Stable Isotopes and the Composition and Origin of Fracture Calcite

Stable isotope analysis of fracture calcite, host-rock dolomite and mud gases reveals information on the source of the fracture-filling fluids and the diagenetic processes at play. δ^{13}C values of fracture calcite (vertical and horizontal) increase down core, however host rock dolomite does not (**Figure 9**). Dolomite formation was an early-stage diagenetic phase (Vaisblat et al., 2017; Liseroudi et al., 2020; Gasparrini et al., 2021) that formed prior to maximum burial and the onset of fracture formation. Therefore, carbon sources for the dolomitizing fluids may have been distinct from those for fracture calcite, however we only have two δ^{13}C values for host rock and more work is needed to fully address this. δ^{13}C values of vertical fracture calcite increases with depth concomitant, and with a similar magnitude to δ^{13}C values of CH$_4$ in mud gas (δ^{13}C values of C2 and C3 also display similar increases down hole, data not shown for clarity). Horizontal-fracture calcite δ^{13}C values also increase with depth, but with a greater deviation, indicating different carbon sources for cements

in these two fracture types. The observed isotopic depth profile for hydrocarbon gases is representative for gradually increasing maturation of thermogenic gases (James, 1983; Schoell, 1983; Chung et al., 1988; Tilley and Muehlenbachs, 2006). Ethane-propane δ^{13}C relationships are consistent with primary cracking of type II kerogen, as measured in mud gases within the WCSB (Tilley and Muehlenbach, 2006). Tandem increases in the δ^{13}C values of fracture calcite suggests depth-related processes also affected fracture calcite δ^{13}C composition. δ^{13}C values in both vertical- and horizontal-fracture calcite increase with depth, however the magnitude of increase is greater in horizontal fracture calcite owing to the timing of calcite precipitation and associated physio-chemical conditions. From fluid-inclusion analysis, as discussed above, we know that vertical and horizontal fractures developed at different times, however, both at elevated temperatures. The negative δ^{13}C values of vertical fracture calcite, in combination with negative δ^{18}O values, is consistent with thermocatalytic decarboxylation and precipitation of carbonates at elevated temperatures in a diagenetic environment (Irwin et al., 1977; Klein et al., 1999; Dale et al., 2014). Increases in the δ^{13}C values of mud-gas CH$_4$ caused by depth-related thermal maturity trends supports the depth-temperature interpretation of fracture calcite δ^{13}C values.

Enhanced down-core enrichments in δ^{13}C values of horizontal fracture calcite (compared with vertical fracture calcite) is likely produced by methanogenesis related to thermochemical production of CH$_4$ associated with hydrocarbon degradation (e.g., Hudson, 1977). CO$_2$ within natural gas systems that is in equilibrium with methane becomes enriched in ^{13}C, which is then incorporated into the carbonate pool (Hudson, 1977), and ultimately into horizontal fracture calcite reflected by increasing δ^{13}C values. Hydrocarbon cracking, gas formation, and the development of overpressure at peak burial combined to enhance the incorporation of methanogenesis-equilibrated carbon in horizontal calcite producing down core enrichments in δ^{13}C values compared with vertical fracture calcite.

δ^{18}O values of vertical and horizontal fracture calcite are similar to host-rock dolomite values, indicating that the oxygen in fracture calcite was likely sourced from host-rock pore fluids (**Figure 9**). At the boundary with the Doig Formation (<1950 m), δ^{18}O values of host rock and fracture calcite are elevated compared with Montney samples (**Figure 9**). Below this depth, δ^{18}O values of both vertical- and horizontal-fracture calcite do not change significantly with depth (except one sample) indicating a similar source of oxygen for all fracture-filling carbonate. The δ^{18}O of pore water (data from operator) is plotted alongside fracture calcite δ^{18}O and displays an increase in δ^{18}O values at the Doig boundary, concomitant with δ^{18}O values in fracture calcite. Further evidence that locally sourced (not migrated) fluids are responsible for precipitation of calcite in fractures. Gasparrini et al. (2021) also noted the similarities in geochemical and petrographic (e.g., cathodoluminescence) characteristics of the fracture calcite and suggested locally sourced parent fluids. To further investigate the source and relationship between fracture calcite and pore water we have modeled the oxygen isotope composition of the parent fluids to compare with the measured pore water composition.
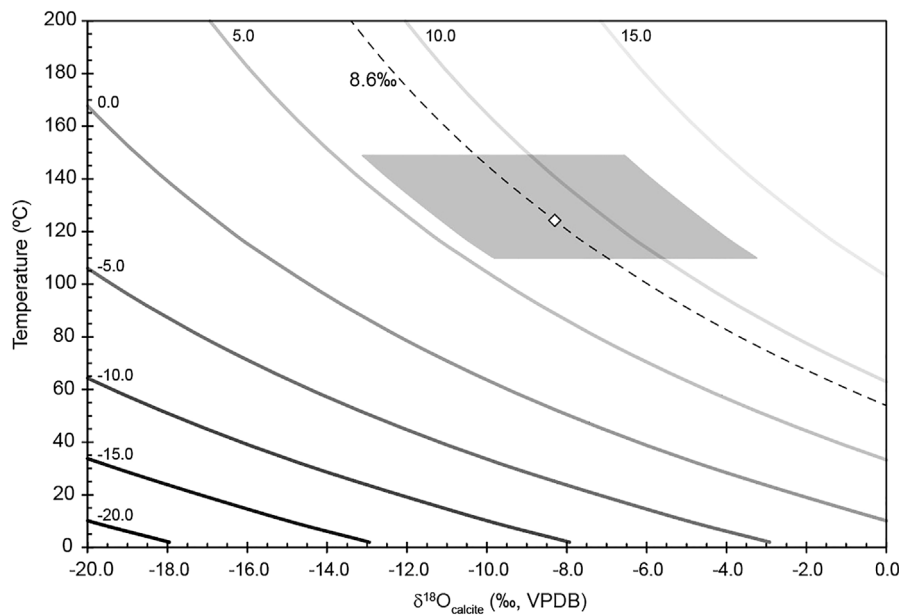
FIGURE 13 | Modelling the $\delta^{18}O$ value of water from which the calcite in the vertical fractures precipitated using fluid inclusion microthermometry and carbonate oxygen isotopes values. Limits of Montney water model $\delta^{18}O$ envelope shown in grey are: +5.7‰ to +12.5‰, with an average value of +8.6‰, dashed line. Temperature limits are 110°C–149.4°C with an average homogenization temperature (123.9°C) and calcite $\delta^{18}O$ value (-8.3‰) shown as diamond.

5.2.1 Modelling the $\delta^{18}O$ Composition of Fracture Calcite Parent Fluids

Combining aqueous inclusion trapping temperatures derived from the measured homogenization temperatures (Th) with measured calcite $\delta^{18}O_{carb}$ values, the $\delta^{18}O_{H2O}$ value of the parent fluid can be calculated (e.g., Blyth et al., 2000; Morad et al., 2010; Ardakani et al., 2013). Homogenization temperatures range from 110 to 149°C, with an average value of 123.9 ± 12.1°C; and $\delta^{18}O_{carb}$ values of vein calcite range from –9.9‰ to –6.6‰ VPDB, with an average value of –8.3 ± 1.5‰ VPDB. Using the high-temperature equilibrium fractionation equation for oxygen isotopes in carbonates (Kim and O'Neil, 1997), the oxygen isotope composition of the parent fluid is calculated to range from +5.7‰ to +12.5‰ VSMOW, with an average value of 8.6‰ VSMOW (**Figure 13**). This range in modeled $\delta^{18}O_{H2O}$ values derived from aqueous inclusions agrees well with measured $\delta^{18}O_{H2O}$ values from pore waters (**Figure 13**). Therefore compositionally, water within aqueous fluid inclusions appear to be in equilibrium with formation pore waters, but have clearly evolved significantly from original Triassic seawater (Veizer et al., 1999). This suggests that carbonate for calcite precipitation was likely derived locally, from pore water, and not from migrated fluids, indicating closed system behavior. This is in agreement with the evidence from the host-rock dolomite-fracture calcite $\delta^{18}O$ relationship described above including previous interpretations (Gasparrini et al., 2021) and with carbon isotope records of hydrocarbon gases within the Montney (Cesar et al., 2020).

The ^{18}O-enriched parent fluids modeled from aqueous fluid inclusions and those measured for pore waters are similar to $\delta^{18}O$ values measured in other Montney formation waters (Osselin et al., 2018; Owen et al., 2020). The NaCl-CaCl$_2$ brine composition (19%

NaCl equiv.) and elevated $\delta^{18}O$ values (compared with seawater) are similar to those observed in Devonian formation waters of the WCSB (**Figure 14**; Simpson, 1999). Ca-Cl brines are thought to reflect interactions of brines with Precambrian basement rocks, which provided important sources of Ca^{2+} and Mg^{2+} and which were potentially involved in the precipitation of dolomite cements (Spencer, 1987). However, vertical migration of fluids seems unlikely due to pervasive bedding-plane parallel permeability barriers and a lack of evidence for vertical homogenization of hydrocarbons (Watt et al., 2022). Clearly, Montney Formation pore fluids evolved from a Triassic seawater composition into Devonian-like brines prior to the development the low permeability conditions that currently exist. However, as vertical migration of fluids is unlikely we speculate that pore water brines formed via evaporative processes within the WCSB similar to those responsible for the evolution of Devonian pore waters (Connolly et al., 1990).

Fluid inclusion analysis and stable isotope geochemistry of fracture calcite and dolomite cements provide evidence that low permeability conditions existed during peak burial associated with the Laramide orogeny. The timing of when low permeability conditions developed is beyond the scope of this study, but likely occurred very early following deposition (Watt et al., 2022). Perhaps future studies on the evolution of dolomite cementation in the Montney will shed light on this intriguing question.

5.3 Implications of Closed System Behaviour

Understanding whether hydrocarbons are dominantly primary and the reservoir is self-sourced (e.g. Ardakani

et al., 2020; Becerra et al., 2020; Ardakani et al., 2021; Euzen et al., 2021), or if hydrocarbons migrated into this system prior to the development of low permeability conditions (e.g., Sanei et al., 2015; Wood et al., 2018; Watt et al., 2022) is of high importance for reservoir evaluation. Similarities in the oxygen isotope analysis of pore waters and the modeled oxygen isotope value of calcite parent fluids implicate closed-system like behavior during the cementation of vertical fractures. Similar findings by a previous fluid inclusion study (Gasparrini et al., 2021) corroborate this interpretation, which may have significant implications for the emplacement of hydrocarbons within the reservoir. Bed-parallel permeability barriers potentially implicate eastward migration of hydrocarbons from a downdip source (Laycock et al., 2021; Watt et al., 2022). However, hydrocarbon migration must predate burial during the Laramide orogeny as these hydrocarbons would need to be in place prior to thermal degradation associated with this burial event. Alternatively, the Montney Formation could represent a hybrid reservoir with a combination of self-sourced and migrated organic matter (Euzen et al., 2021; Ardakani et al., 2020).

Nonetheless, the closed system behavior and subsequent development of overpressure associated with thermal degradation of hydrocarbons resulted in the formation of bedding-plane parallel fractures and the brecciated horizons, potentially in concert with local tectonic activity. Therefore formation of these fractures is directly related to the generation of light hydrocarbon-rich (condensate) fluids found in the petroleum inclusions (shown in this study)

and currently produced from this well. In addition, the persistence of overpressure is indicative that the fracture system has done little to promote substantial fluid flow or enhance permeability in the reservoir.

Interest in the characteristics of fluid migration within fine grain siltstone reservoirs is pertinent as these types of formations are increasingly exploited for hydrocarbon production. Fluid inclusion studies of fractures within these systems play an important part in evaluating the potential role fractures play in fluid migration and enhancing permeability in these low permeability systems. The combined use of fluid inclusion microthermometry, stable isotope geochemistry, and Raman spectroscopy will be essential in the accurate evaluation of fluid flow within low permeability reservoirs and ultimately understanding their complex diagenetic history.

6 CONCLUSION

In this study we used fluid inclusion and geochemical techniques to better constrain the origin, timing and evolution of fluids in a complex diagenetic system. The Montney Formation has undergone multiple periods of burial and uplift related to regional tectonic activity. Associated with tectonism was the development of calcite-filled fractures resulting in an archive of fluid flow events. Differences between the characteristics of co-occurring, but not cogenetic, aqueous and petroleum fluid inclusions provide a record of these events and help elucidate the timing of
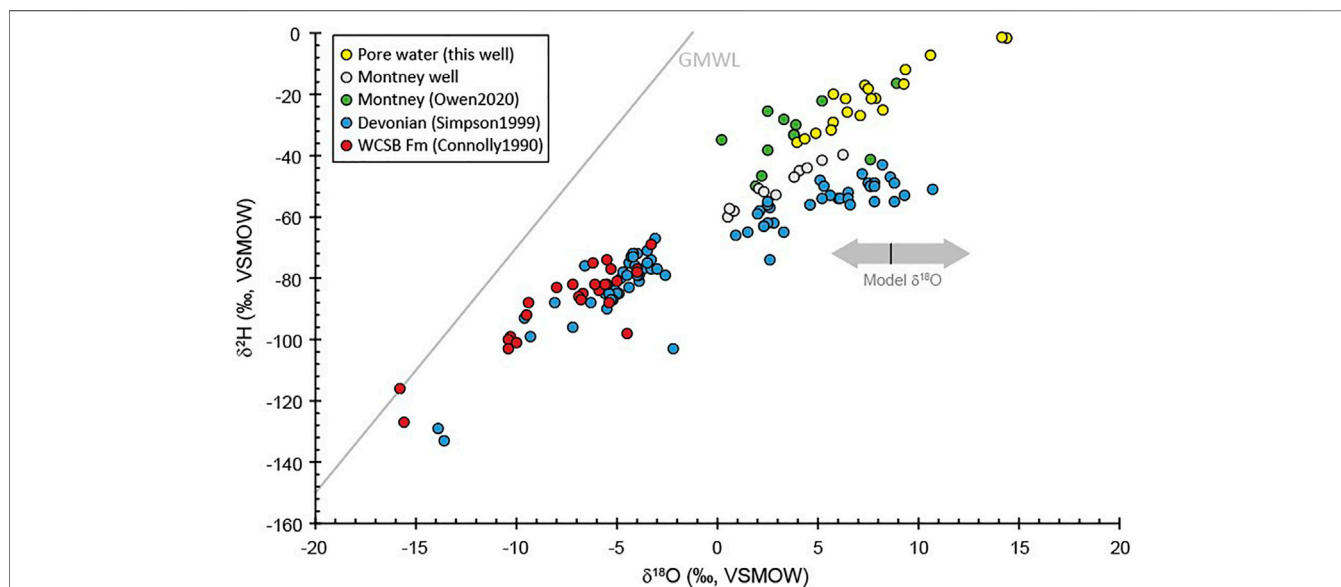
FIGURE 14 | Stable isotope values from Western Canadian Sedimentary Basin (WCSB) formation waters and modeled water from Montney vertical fracture calcite. Isotope analysis from this well (yellow) and another Montney well (grey) are from pore waters extracted from cores. Montney waters from Owen et al. (2020) were derived from flowback waters. WCSB Fm. waters (Connolly et al., 1990) include Devonian, Mississippian, Jurassic, and Cretaceous formation waters, but dominantly Mesozoic formation waters.

hydrocarbon maturation and migration within the basin. The main conclusions of this study are:

- The formation of vertical, bedding-plane parallel and brecciated fractures occurred over a short interval during and immediately proceeding the timing of maximum burial. The lack of hydrocarbons in aqueous fluid inclusions indicates hydrocarbons were absent or in low abundance within the earliest fluids, which formed the vertical fracture system. Bedding-plane parallel and brecciated fractures postdate vertical fractures and secondary petroleum inclusions within vertical fractions represent a reactivation of this existing fracture network.
- Aqueous fluid inclusions formed at elevated temperatures and pressure likely close to the period of maximum burial associated with the Laramide orogeny based on modeled trapping temperatures ~142°C and burial history models.
- Pressure-temperature modeling of petroleum inclusions indicates formation pressures approaching or exceeding lithostatic pressure, which is consistent with the development overpressure and the formation of bedding-plane parallel fractures. Petroleum inclusions record lower and more consistent homogenization temperatures (~45°C), have a small range in vapor fractions, and monochromatic fluorescence color under UV illumination. These similarities suggest synchronous and homogeneous formation despite occurring over a depth range of 216 m.

DATA AVAILABILITY STATEMENT

The original contributions presented in the study are included in the article/supplementary material, further inquiries can be directed to the corresponding author.

AUTHOR CONTRIBUTIONS

AK and OA designed the project. AK, OA, and EW collected samples. AK conducted all analysis. All authors interpreted results. AK, OA, and IS wrote the manuscript. All authors edited the manuscript.

REFERENCES

Adam, J. (2000). *Lithofacies and Geochemistry of Carbonates in the Late Devonian Duvernay Formation of Central Alberta. Unpublished.* B. Sc. Thesis, University of Windsor, 66p

Al-Aasm, I. S., and Clarke, J. D. (2004). "The Effect of Hydrothermal Fluid Flow on Early Diagenetic Dolomitization: an Example from the Devonian Slave Point Formation, Northwest Alberta, Canada," in *Deformation, Fluid Flow, and Reservoir Appraisal in Foreland Fold and Thrust Belts: AAPG Hedberg Series, No. 1.* Editors R. Swennen, F. Roure, and J. W. Granath (Tulsa, Okla: American Association of Petroleum Geologists), 297

Al-Aasm, I. S., Mrad, C., and Packard, J. (2019). Fluid Compartmentalization of Devonian and Mississippian Dolostones, Western Canada Sedimentary Basin: Petrologic and Geochemical Evidence from Fracture Mineralization. *Can. J. Earth Sci.* 56 (3), 265–305. doi:10.1139/cjes-2018-0226

Aplin, A. c., Macleod, G., Larter, S. R., Pedersen, K. S., Sorensen, H., and Booth, T. (1999). Combined Use of Confocal Laser Scanning Microscopyand PVT Simulation for Estimating the Composition Andphysical Properties of Petroleum in Fluid Inclusions. *Mar. Petroleum Geol.* 16 (2), 97–110. doi:10.1016/s0264-8172(98)00079-8

Ardakani, O. H., Becerra, D., Mackie, S. J., Pedersen, P. K., Reyes, J., Wood, J. M., et al. (2020b). Organic Matter in the Alberta Montney Re-visited: Evidence for Primary Organic Matter and Local Hydrocarbon Migration. *Geoconvention*

Bakker, R. J. (2018). AqSo_NaCl: Computer Program to Calculate P-T-V-X Properties in the H_2O-NaCl Fluid System Applied to Fluid Inclusion Research and Pore Fluid Calculation. *Comput. Geosciences* 115, 122–133. doi:10.1016/j.cageo.2018.03.003

Barclay, J. E., Krause, F. F., Campbell, R. I., and Utting, J. (1990). Dynamic Casting of Growth Faulting: Dawson Creek Graben Complex, Carboniferous-Permian Peace River Embayment. *West. Bull. Can. Petroleum Geol.* 38A, 115

Becerra, D., Clarkson, C. R., Ghanizadeh, A., and Ardakani, O. H. (2020). First-Time Characterization of Black Shaly Facies along a Full Montney Core: Lithofacies Controls on the Distribution of Primary Organic Matter. *Geoconvention*. Virtual Event.

Berger, Z., Boast, M., and Mushayandebvu, M. (2008). The Contribution of Integrated HRAM Studies to Exploration and Exploitation of Unconventional Plays in North America Part 1. *Peace River Arch Reserv.* 35, 42

Blyth, A., Frape, S., Blomqvist, R., and Nissinen, P. (2000). Assessing the Past Thermal and Chemical History of Fluids in Crystalline Rock by Combining Fluid Inclusion and Isotopic Investigations of Fracture Calcite. *Appl. Geochem.* 15 (10), 1417–1437. doi:10.1016/s0883-2927(00)00007-x

Bodnar, R. J. (2003). Introduction to Aqueous-Electrolyte Fluid Inclusions. *Fluid inclusions Analysis interpretation* 32, 81

Bodnar, R. J. (1993). Revised Equation and Table for Determining the Freezing Point Depression of H2O-Nacl Solutions. *Geochimica Cosmochimica acta* 57 (3), 683–684. doi:10.1016/0016-7037(93)90378-a

Bourdet, J., Burruss, R. C., Chou, I.-M., Kempton, R., Liu, K., and Hung, N. V. (2014). Evidence for a Palaeo-Oil Column and Alteration of Residual Oil in a Gas-Condensate Field: Integrated Oil Inclusion and Experimental Results. *Geochimica Cosmochimica Acta* 142, 362–385. doi:10.1016/j.gca.2014.07.022

Brand, W. A., Coplen, T. B., Vogl, J., Rosner, M., and Prohaska, T. (2014). Assessment of International Reference Materials for Isotope-Ratio Analysis (IUPAC Technical Report). *Pure Appl. Chem.* 86 (3), 425–467. doi:10.1515/pac-2013-1023

Burruss, R. C., Slepkov, A. D., Pegoraro, A. F., and Stolow, A. (2012). Unraveling the Complexity of Deep Gas Accumulations with Three-Dimensional

Multimodal CARS Microscopy. *Geology* 40 (12), 1063–1066. doi:10.1130/g33321.1

Cesar, J., Nightingale, M., Becker, V., and Mayer, B. (2020). Stable Carbon Isotope Systematics of Methane, Ethane and Propane from Low-Permeability Hydrocarbon Reservoirs. *Chem. Geol.* 558, 119907. doi:10.1016/j.chemgeo.2020.119907

Chen, Y., Steele-MacInnis, M., Ge, Y., Zhou, Z., and Zhou, Y. (2016). Synthetic Saline-Aqueous and Hydrocarbon Fluid Inclusions Trapped in Calcite at Temperatures and Pressures Relevant to Hydrocarbon Basins: A Reconnaissance Study. *Mar. Petroleum Geol.* 76, 88–97. doi:10.1016/j.marpetgeo.2016.05.015

Chou, I.-M., Song, Y., and Burruss, R. C. (2008). A New Method for Synthesizing Fluid Inclusions in Fused Silica Capillaries Containing Organic and Inorganic Material. *Geochimica Cosmochimica Acta* 72 (21), 5217–5231. doi:10.1016/j.gca.2008.07.030

Chung, H. M., Gormly, J. R., and Squires, R. M. (1988). Origin of Gaseous Hydrocarbons in Subsurface Environments: Theoretical Considerations of Carbon Isotope Distribution. *Chem. Geol.* 71, 97–104. doi:10.1016/0009-2541(88)90108-8

Cobbold, P. R., Zanella, A., Rodrigues, N., and Løseth, H. (2013). Bedding-parallel Fibrous Veins (Beef and Cone-In-Cone): Worldwide Occurrence and Possible Significance in Terms of Fluid Overpressure, Hydrocarbon Generation and Mineralization. *Mar. Petroleum Geol.* 43, 1–20. doi:10.1016/j.marpetgeo.2013.01.010

Connolly, C. A., Walter, L. M., Baadsgaard, H., and Longstaffe, F. J. (1990). Origin and Evolution of Formation Waters, Alberta Basin, Western Canada Sedimentary Basin. II. Isotope Systematics and Water Mixing. *Appl. Geochem.* 5 (4), 397–413. doi:10.1016/0883-2927(90)90017-y

Cosgrove, J. W. (1995). *The Expression of Hydraulic Fracturing in Rocks and Sediments*. London: Geological Society, Special Publications Vol. 92 (1), 187–196.

Davies, G. R., Moslow, T. F., and Sherwin, M. D. (1997). The Lower Triassic Montney Formation, West-Central Alberta. *Bull. Can. Petroleum Geol.* 45 (4), 474–505. doi:10.35767/gscpgbull.45.4.474

Davies, G. R., and Smith, L. B. (2006). Structurally Controlled Hydrothermal Dolomite Reservoir Facies: An Overview. *Bulletin* 90 (11), 1641–1690. doi:10.1306/05220605164

Davies, G. R. (1997). The Triassic of the Western Canada Sedimentary Basin: Tectonic and Stratigraphic Framework, Paleogeography, Paleoclimate and Biota. *Bull. Can. Petroleum Geol.* 45 (4), 434–460. doi:10.35767/gscpgbull.45.4.434

Davies, G. R., Watson, N., Moslow, T. F., and Maceachern, J. A. (2018). Regional Subdivisions, Sequences, Correlations and Facies Relationships of the Lower Triassic Montney Formation, West-Central Alberta to Northeastern British Columbia, Canada-With Emphasis on Role of Paleostructure. *Bull. Can. Petroleum Geol.* 66, 23

Ducros, M., Sassi, W., Vially, R., Euzen, T., and Crombez, V. (2017). "2-D Basin Modeling of the Western Canada Sedimentary Basin across the Montney-Doig System: Implications for Hydrocarbon Migration Pathways and Unconventional Resources Potential," in *Petroleum Systems Analysis—Case Studies: AAPG Memoir 114*. Editors M. A. AbuAli, I. Moretti, M. Hege, and N. Bolås, 117

Euzen, T., Watson, N., Fowler, M., Mort, A., and Moslow, T. F. (2021). Petroleum Distribution in the Montney Hybrid Play: Source, Carrier Bed, and Structural Controls. *Bulletin* 105 (9), 1867–1892. doi:10.1306/12222020088

Fabre, D., and Couty, R. (1986). Etude, par spectroscopie Raman, du méthane comprimé jusqu'à 3 kbar. Application à la mesure de pression dans les inclusions fluides contenues dans les minéraux. *Comptes rendus l'Académie Sci. Série 2, Mécanique, Phys. Chim. Sci. l'univers, Sci. Terre* 303 (14), 1305

Frezzotti, M. L., Tecce, F., and Casagli, A. (2012). Raman Spectroscopy for Fluid Inclusion Analysis. *J. Geochem. Explor.* 112, 1–20. doi:10.1016/j.gexplo.2011.09.009

Gao, J., He, S., Zhao, J.-x., and Yi, J. (2017). Geothermometry and Geobarometry of Overpressured Lower Paleozoic Gas Shales in the Jiaoshiba Field, Central China: Insight from Fluid Inclusions in Fracture Cements. *Mar. Petroleum Geol.* 83, 124–139. doi:10.1016/j.marpetgeo.2017.02.018

Gasparrini, M., Lacombe, O., Rohais, S., Belkacemi, M., and Euzen, T. (2021). Natural Mineralized Fractures from the Montney-Doig Unconventional Reservoirs (Western Canada Sedimentary Basin): Timing and Controlling

Factors. *Mar. Petroleum Geol.* 124, 104826. doi:10.1016/j.marpetgeo.2020.104826

Ghanizadeh, A., Clarkson, C. R., Aquino, S., Ardakani, O. H., and Sanei, H. (2015). Petrophysical and Geomechanical Characteristics of Canadian Tight Oil and Liquid-Rich Gas Reservoirs: I. Pore Network and Permeability Characterization. *Fuel* 153, 664–681. doi:10.1016/j.fuel.2015.03.020

Gibbs, A., and Rakhit, K. (2019). "Hydrodynamics, Geothermics and Spatial Variations in Hydrocarbon Fluid Distribution within the Montney Formation," in *SPE Annual Technical Conference and Exhibition, Calgary, AB, September 2019* (Canada: Alberta and British Columbia). doi:10.2118/196101-MS

Goldstein, R. H., and Reynolds, T. J. (1994). *Fluid Inclusion Microthermometry*.

Golonka, J. (2007). Late Triassic and Early Jurassic Palaeogeography of the World. *Palaeogeogr. Palaeoclimatol. Palaeoecol.* 244, 297–307. doi:10.1016/j.palaeo.2006.06.041

Haeri-Ardakani, O., Al-Aasm, I., and Coniglio, M. (2013). Petrologic and Geochemical Attributes of Fracture-Related Dolomitization in Ordovician Carbonates and Their Spatial Distribution in Southwestern Ontario, Canada. *Mar. Petroleum Geol.* 43, 409–422. doi:10.1016/j.marpetgeo.2012.12.006

Hansen, S. B., Berg, R. W., and Stenby, E. H. (2001). Raman Spectroscopic Studies of Methane-Ethane Mixtures as a Function of Pressure. *Appl. Spectrosc.* 55 (6), 745–749. doi:10.1366/0003702011952442

Henry, D. G., Jarvis, I., Gillmore, G., and Stephenson, M. (2019). Raman Spectroscopy as a Tool to Determine the Thermal Maturity of Organic Matter: Application to Sedimentary, Metamorphic and Structural Geology. *Earth-Science Rev.* 198, 102936. doi:10.1016/j.earscirev.2019.102936

Hope, J., Eaton, D. W., and Ross, G. M. (1999). Lithoprobe Seismic Transect of the Alberta Basin: Compilation and Overview. *Bull. Can. Petroleum Geol.* 47, 331

Hubbert, M. K., and Willis, D. G. (1957)., Mechanics of Hydraulic Fracturing. *Transaction Am. Inst. Min. Metallurgical, Petroleum Eng. Incorporated.* 210, 153–168. doi:10.2118/686-g

Hudson, J. D. (1977). Stable Isotopes and Limestone Lithification. *J. Geol. Soc.* 133 (6), 637–660. doi:10.1144/gsjgs.133.6.0637

Irwin, H., Curtis, C., and Coleman, M. (1977). Isotopic Evidence for Source of Diagenetic Carbonates Formed during Burial of Organic-Rich Sediments. *Nature* 269 (5625), 209–213. doi:10.1038/269209a0

James, A. T. (1983). Correlation of Natural Gas by Use of Carbon Isotope Distribution between Hydrocarbon Components. *Am. Assoc. Petroleum Geol. Bull.* 67, 1176–1191. doi:10.1306/03b5b722-16d1-11d7-8645000102c1865d

Kim, S.-T., and O'Neil, J. R. (1997). Equilibrium and Nonequilibrium Oxygen Isotope Effects in Synthetic Carbonates. *Geochimica cosmochimica acta* 61 (16), 3461–3475. doi:10.1016/s0016-7037(97)00169-5

Lai, J., Liu, B., Li, H., Pang, X., Liu, S., Bao, M., et al. (2021). Bedding Parallel Fractures in Fine-Grained Sedimentary Rocks: Recognition, Formation Mechanisms, and Prediction Using Well Log. *Petroleum Sci.*

Laycock, D., Watt, E., Tobin, R., Kelly, S., Johnston, M., and Michael, E. (2021). "July. Examining the Origins and Yield Impact of a Stratified Oil Column in the Montney Formation, NE BC," in *SPE/AAPG/SEG Unconventional Resources Technology Conference.*

Lin, F., Bodnar, R. J., and Becker, S. P. (2007). Experimental Determination of the Raman CH_4 Symmetric Stretching (v1) Band Position from 1-650bar and 0.3-22°C: Application to Fluid Inclusion Studies. *Geochimica Cosmochimica Acta* 71 (15), 3746–3756. doi:10.1016/j.gca.2007.05.016

Liseroudi, M. H., Ardakani, O. H., Pedersen, P. K., Stern, R. A., Wood, J. M., and Sanei, H. (2021). Microbial and Thermochemical Controlled Sulfur Cycle in the Early Triassic Sediments of the Western Canadian Sedimentary Basin. *J. Geol. Soc.* 178 (1), jgs2020–175. doi:10.1144/jgs2020-175

Liseroudi, M. H., Ardakani, O. H., Sanei, H., Pedersen, P. K., Stern, R. A., and Wood, J. M. (2020). Origin of Sulfate-Rich Fluids in the Early Triassic Montney Formation, Western Canadian Sedimentary Basin. *Mar. Petroleum Geol.* 114, 104236. doi:10.1016/j.marpetgeo.2020.104236

Lu, W., Chou, I.-M., Burruss, R. C., and Song, Y. (2007). A Unified Equation for Calculating Methane Vapor Pressures in the CH_4-H_2O System with Measured Raman Shifts. *Geochimica Cosmochimica Acta* 71 (16), 3969–3978. doi:10.1016/j.gca.2007.06.004

Mei, S. (2009). New Insights on Faults in the Peace River Arch Region, Northwest Alberta, Based on Existing Well-Log Data and Refined Trend Surface Analysis. *Can. J. Earth Sci.* 46, 41–65. doi:10.1139/e09-006

Morad, S., Al-Aasm, I. S., Sirat, M., and Sattar, M. M. (2010). Vein Calcite in Cretaceous Carbonate Reservoirs of Abu Dhabi: Record of Origin of Fluids and Diagenetic Conditions. *J. Geochem. Explor.* 106 (1-3), 156–170. doi:10.1016/j.gexplo.2010.03.002

Munz, I. A. (2001). Petroleum Inclusions in Sedimentary Basins: Systematics, Analytical Methods and Applications. *Lithos* 55 (1-4), 195

National Research Council (1996). *Rock Fractures and Fluid Flow: Contemporary Understanding and Applications*. Washington, DC: The National Academies Press. doi:10.17226/2309

Ness, S. M. (2001). "The Application of Basin Analysis to the Triassic Succession, Alberta Basin: an Investigation of Burial and Thermal History and Evolution of Hydrocarbons," in *Triassic Rocks (M.Sc. Thesis)* (Canada: University of Calgary), 192.

O'Connell, S. C., Dixon, G. R., and Barclay, J. E. (1990). The Origin, History, and Regional Structural Development of the Peace River Arch, Western Canada. *Bull. Can. Petroleum Geol.* 38A, 4

Osselin, F., Nightingale, M., Hearn, G., Kloppmann, W., Gaucher, E., Clarkson, C. R., et al. (2018). Quantifying the Extent of Flowback of Hydraulic Fracturing Fluids Using Chemical and Isotopic Tracer Approaches. *Appl. Geochem.* 93, 20–29. doi:10.1016/j.apgeochem.2018.03.008

Owen, J., Bustin, R. M., and Bustin, A. M. M. (2020). Insights from Mixing Calculations and Geochemical Modeling of Montney Formation Post Hydraulic Fracturing Flowback Water Chemistry. *J. Petroleum Sci. Eng.* 195, 107589. doi:10.1016/j.petrol.2020.107589

Pan , D. I., and van der Pluijm, B. A. (2014). Orogenic Pulses in the Alberta Rocky Mountains: Radiometric Dating of Major Faults and Comparison with the Regional Tectono-Stratigraphic Record. *Geol. Soc. Am. Bull.* 127, 480–502. doi:10.1130/B31069.1

Pironon, J., and Bourdet, J. (2008). Petroleum and Aqueous Inclusions from Deeply Buried Reservoirs: Experimental Simulations and Consequences for Overpressure Estimates. *Geochimica Cosmochimica Acta* 72 (20), 4916–4928. doi:10.1016/j.gca.2008.07.019

Price, R. (1994). "Cordilleran Tectonics and the Evolution of the Western Canada Sedimentary Basin," in *Geological Atlas of Western Canada. G.D. Mossop and I. Shetsen (Comps.). Calgary* (Canadian Society of Petroleum Geologists/Alberta Research CouncilUniversity of Windsor), 13156

Rivas, D. (2004). *Dolomitization of the Devonian Wabamun Carbonates in the Gold Creek Field West Central Alberta, Canada*. Unpublished: M.Sc. thesisUniversity of Windsor, 156.

Rodrigues, N., Cobbold, P. R., Loseth, H., and Ruffet, G. (2009). Widespread Bedding-Parallel Veins of Fibrous Calcite ('beef') in a Mature Source Rock (Vaca Muerta Fm, Neuquén Basin, Argentina): Evidence for Overpressure and Horizontal Compression. *J. Geol. Soc.* 166 (4), 695–709. doi:10.1144/0016-76492008-111

Roedder, E. (1984). Volume 12: Fluid Inclusions. *Rev. mineralogy* 12.

Rohais, S., Crombez, V., Euzen, T., and Zonneveld, J. P. (2018). Subsidence Dynamics of the Montney Formation (Early Triassic, Western Canada Sedimentary Basin): Insights for its Geodynamic Setting and Wider Implications. *Bull. Can. Petroleum Geol.* 66, 128

Rongxi, L., Guzmics, T., Xiaojie, L., and Guangcheng, X. (2011). Migration of Immiscible Hydrocarbons Recorded in Calcite-Hosted Fluid Inclusions, Ordos Basin: a Case Study from Northern China. *Russ. Geol. Geophys.* 52 (11), 1491–1503. doi:10.1016/j.rgg.2011.10.016

Rosenbaum, J., and Sheppard, S. M. F. (1986). An Isotopic Study of Siderites, Dolomites and Ankerites at High Temperatures. *Geochimica cosmochimica acta* 50 (6), 1147–1150. doi:10.1016/0016-7037(86)90396-0

Ruble, T. E., George, S. C., Lisk, M., and Quezada, R. A. (1998). Organic Compounds Trapped in Aqueous Fluid Inclusions. *Org. Geochem.* 29 (1-3), 195–205. doi:10.1016/s0146-6380(98)00090-4

Sanei, H., Wood, J. M., Ardakani, O. H., Clarkson, C. R., and Jiang, C. (2015). Characterization of Organic Matter Fractions in an Unconventional Tight Gas Siltstone Reservoir. *Int. J. Coal Geol.* 150-151 (151), 296–305. doi:10.1016/j.coal.2015.04.004

Schoell, M. (1983). Genetic Characterization of Natural Gases. *Am. Assoc. Petroleum Geol. Bull.* 67, 2225–2238. doi:10.1306/03b5b4c5-16d1-11d7-8645000102c1865d

Simpson, G. P. (1999). *Sulfate Reduction and Fluid Chemistry of the Devonian, Leduc and Nisku Formations in South-Central Alberta*. Ph.D. Thesis. Calgary: University of Calgary PhD Thesis, 228.

Spencer, R. J. (1987). Origin of CaCl Brines in Devonian Formations, Western Canada Sedimentary Basin. *Appl. Geochem.* 2 (4), 373–384. doi:10.1016/0883-2927(87)90022-9

Sum, A. K., Burruss, R. C., and Sloan, E. D. (1997). Measurement of Clathrate Hydrates via Raman Spectroscopy. *J. Phys. Chem. B* 101 (38), 7371–7377. doi:10.1021/jp970768e

Tilley, B., and Muehlenbachs, K. (2006). Gas Maturity and Alteration Systematics across the Western Canada Sedimentary Basin from Four Mud Gas Isotope Depth Profiles. *Org. Geochem.* 37 (12), 1857–1868. doi:10.1016/j.orggeochem.2006.08.010

Tufano, B. C., and Pietras, J. T. (2017). Coupled Flexural-Dynamic Subsidence Modeling Approach for Retro-Foreland Basins: Example from the Western Canada Sedimentary Basin. *Bulletin* 129 (11-12), 1622–1635. doi:10.1130/b31646.1

Vaisblat, N., Harris, N. B., Ayranci, K., Power, M., DeBhur, C., Bish, D. L., et al. (2021). Compositional and Diagenetic Evolution of a Siltstone, with Implications for Reservoir Quality; an Example from the Lower Triassic Montney Formation in Western Canada. *Mar. Petroleum Geol.* 129, 105066. doi:10.1016/J.MARPETGEO.2021.105066

Vaisblat, N., Harris, N. B., DeBuhr, C., Euzen, T., Gasparrini, M., Crombez, M., et al. (2017). Diagenetic Model for the Deep Montney Formation, Northeastern British Columbia. *Geoscience BC Summary of Activities* 2016, 2017.

Veizer, J., Ala, D., Azmy, K., Bruckschen, P., Buhl, D., Bruhn, F., et al. (1999). 87Sr/86Sr, δ13C and δ18O Evolution of Phanerozoic Seawater. *Chem. Geol.* 161 (1-3), 59–88. doi:10.1016/s0009-2541(99)00081-9

Volk, H., and George, S. C. (2019). Using Petroleum Inclusions to Trace Petroleum Systems - A Review. *Org. Geochem.* 129, 99–123. doi:10.1016/j.orggeochem.2019.01.012

Watt, E. A., Laycock, D. P., Michael, E., Tobin, R. C., Kelly, S., and Johnston, M. N. (2022). Hydrocarbon Charge and Petroleum System Evolution of the Montney Formation: A Multidisciplinary Case Study of the Blueberry Sub-play in Northeast. *Bull. Can. Energy Geoscience* 69 (1), 21

Weides, S., and Majorowicz, J. (2014). Implications of Spatial Variability in Heat Flow for Geothermal Resource Evaluation in Large Foreland Basins: the Case of the Western Canada Sedimentary Basin. *Energies* 7 (4), 2573–2594. doi:10.3390/en7042573

Wood, J. M., and Sanei, H. (2016). Secondary Migration and Leakage of Methane from a Major Tight-Gas System. *Nat. Commun.* 7 (1), 13614–13619. doi:10.1038/ncomms13614

Wood, J. M., Sanei, H., Haeri-Ardakani, O., Curtis, M. E., Akai, T., and Currie, C. (2018). Solid Bitumen in the Montney Formation: Diagnostic Petrographic Characteristics and Significance for Hydrocarbon Migration. *Int. J. Coal Geol.* 198, 48–62. doi:10.1016/j.coal.2018.09.004

Wozniakowska, P., Eaton, D. W., Deblonde, C., Mort, A., and Ardakani, O. H. (2021). Identification of Regional Structural Corridors in the Montney Play Using Trend Surface Analysis Combined with Geophysical Imaging, British Columbia and Alberta. *Geol. Surv. Can. Open File* 8814, 202162. doi:10.4095/328850

Wright, G. N., McMechan, M. E., and Potter, D. E. G. (1994). "Structure and Architecture of the Western Canada Sedimentary Basin," in *Geological Atlas of Western Canada. G.D. Mossop and I. Shetsen (Comps.). Calgary* (Canadian Society of Petroleum Geologists/Alberta Research Council), 25.

Zanella, A., Cobbold, P. R., Rodrigues, N., Løseth, H., Jolivet, M., Gouttefangeas, F., et al. (2021). Source Rocks in Foreland Basins: a Preferential Context for the Development of Natural Hydraulic Fractures. *Bulletin* 105 (4), 647–668. doi:10.1306/08122018162

Zhang, J., Qiao, S., Lu, W., Hu, Q., Chen, S., and Liu, Y. (2016). An Equation for Determining Methane Densities in Fluid Inclusions

with Raman Shifts. *J. Geochem. Explor.* 171, 20–28. doi:10.1016/j.gexplo.2015.12.003

Zonneveld, J. P., and Moslow, T. F. (2018). Palaeogeographic Setting, Lithostratigraphy, and Sedimentary Framework of the Lower Triassic Montney Formation of Western Alberta and Northeastern British Columbia. *Bull. Can. Petroleum Geol.* 66, 93

Conflict of Interest: Author EW was employed by ConocoPhilips Canada.

The remaining authors declare that the research was conducted in the absence of any commercial or financial relationships that could be construed as a potential conflict of interest.

Publisher's Note: All claims expressed in this article are solely those of the authors and do not necessarily represent those of their affiliated organizations, or those of the publisher, the editors and the reviewers. Any product that may be evaluated in this article, or claim that may be made by its manufacturer, is not guaranteed or endorsed by the publisher.